Available online at www.sciencedirect.com
SCIENCE DIRECT®
European Journal of Mechanics B/Fluids 25 (2006) 33–58

On two-dimensional linear waves in Blasius boundary layer over viscoelastic layers

Z. Wang [a], K.S. Yeo [b,*], B.C. Khoo [b,c]

[a] *Temasek Laboratories, National University of Singapore, 1 Engineering Drive 2, 117576 Singapore*
[b] *Department of Mechanical Engineering, National University of Singapore, 1 Engineering Drive 2, 117576 Singapore*
[c] *Singapore MIT Alliance, National University of Singapore, 1 Engineering Drive 2, 117576 Singapore*

Received 3 November 2003; received in revised form 18 November 2004; accepted 18 April 2005

Available online 1 June 2005

Abstract

This work concerns the direct numerical simulation of small-amplitude two-dimensional ribbon-excited waves in Blasius boundary layer over viscoelastic compliant layers of finite length. A vorticity-streamfunction formulation is used, which assures divergence-free solutions for the evolving flow fields. Waves in the compliant panels are governed by the viscoelastic Navier's equations. The study shows that Tollmien–Schlichting (TS) waves and compliance-induced flow instability (CIFI) waves that are predicted by linear stability theory frequently coexist on viscoelastic layers of finite length. In general, the behaviour of the waves is consistent with the predictions of linear stability theory. The edges of the compliant panels, where abrupt changes in wall property occur, are an important source of waves when they are subjected to periodic excitation by the flow. The numerical results indicate that the non-parallel effect of boundary-layer growth is destabilizing on the TS instability. It is further demonstrated that viscoelastic layers with suitable properties are able to reduce the amplification of the TS waves, and that high levels of material damping are effective in controlling the propagating CIFI.

Keywords: Boundary-layer flow; Compliant walls; Instabilities; Viscoelastic layer

1. Introduction

Among the many compliant wall models that have been studied so far for their effects on flow stability, volume-based walls such as viscoelastic layers are deemed the most practical because they are simpler to build and implement as compared with surface-based walls. Nonweiler [1], Kaplan [2] and Landahl and Kaplan [3] carried out the first series of theoretical studies on the linear stability of boundary-layer flows past viscoelastic layers in the early 1960s. There was a considerable lull of some two decades before further works was presented by Fraser and Carpenter [4], Yeo [5] and Yeo and Dowling [6], following a renewal of interest in compliant-wall flow stability research. Yeo [7–9] has carried out to date the most comprehensive investigation into the linear stability of Blasius boundary layer over viscoelastic walls; covering two-dimensional (2D) and three-dimensional (3D) wave modes over isotropic and anisotropic single- and multi-layer viscoelastic walls. The effects of flow loading (over-burden pressure) and boundary-layer growth on flow stability were considered by Yeo et al. [10,11]. Meanwhile, the occurrence

* Corresponding author.
E-mail address: mpeyeoks@nus.edu.sg (K.S. Yeo).

0997-7546/$ – see front matter
doi:10.1016/j.euromechflu.2005.04.006

of absolute instability over viscoelastic layers has also been studied by Yeo et al. [12–14], while the optimization of viscoelastic-layered walls for transition delay could be found in Dixon et al. [15] and Yeo [16].

Domaradzki and Metcalfe's [17] performed probably the first direct numerical simulation (DNS) of unstable waves in shear flow over a compliant surface, a tensioned membrane in particular. They employed a spectral method with Fourier and Chebyshev polynomial series applied in the streamwise and normal directions, respectively. Periodic conditions were implemented for the streamwise and spanwise boundaries and the waves were assumed to grow or decay with time. We term this the *temporal DNS* approach here. The temporal DNS of three-dimensional (3D) waves in transitional boundary layers on membrane surfaces was subsequently carried out by Metcalfe et al. [18]. Their simulation showed that non-linear secondary instabilities could arise and cause the flow to become unstable when it was predicted to be stable by the linear theory. On the other hand, the computational simulation of unstable waves in flow over viscoelastic layers appears to have been done only by Hall [19]. Again the temporal wave growth model was used, while the response of the polyvinylchloride (PVC) layers was computed by a finite-element code DYNA2D. Results were obtained for the effects of wall compliance on the Tollmien–Schlichting (TS) waves.

In temporal DNS, the computational domain is normally trimmed down to one or just a few TS fundamental wavelengths in the streamwise direction to conserve computational resources. However, for the accurate determination of unstable waves in boundary layers over finite compliant panels, the temporal model is inapplicable due to the presence of inhomogeneities in the stream direction: the growth of the boundary layer and the leading and trailing edges of the compliant panel, where sharp changes of properties occur. Moreover, Tollmien–Schlichting (TS) and compliance-induced flow instability (CIFI) waves with incompatible wavelengths may co-exist. The imposition of periodic boundary conditions for one wave group may artificially inhibit the existence of the other. These call for the use of a more general spatial treatment. Davies and Carpenter [20] carried out probably the first *spatial DNS* of unstable waves in shear flow over finite compliant panels. A novel vorticity–velocity method was used in the simulations. Using this method with special treatment for the wall and fluid inertial terms, they solved the linearized N-S equations and presented the results for the spatial evolution of TS waves over finite membrane panels. Wiplier and Ehrenstein [21,22] adopted a primitive-variable method for spatial 2D disturbances in boundary layers over membrane panels. The behaviour of the disturbances as convective and absolute instabilities was investigated. Their simulation results re-affirmed the overall validity of the linear stability theory and show that absolute instability could arise from the coalescence between an upstream propagating evanescent mode and a downstream propagating TS wave, as was earlier suggested by Yeo et al. [12]. Their model takes into account the non-parallelism of the flow and non-linear effects within the flow. To handle the moving boundary, the physical domain was transformed into a fixed computational domain. However, as the prescribed base flow was dynamically stretched with the deformation of the compliant boundary, this may introduce inaccuracies in cases where the surface wave amplitude is large. Recently, Davies and Carpenter [23] developed a method for simulating linear wave evolution in 3D boundary layer over compliant surfaces, and applied it to perturbed boundary layers on a rotating disk. Unlike the established 3D vorticity–velocity method, in which six governing equations are usually required, only three governing equations are solved in their highly efficient formulation. The linearized form of this method was validated for convective instabilities evolving over rigid and compliant rotating discs. More recently, Wang [24] proposed a 3D primitive variable method for simulating transitional boundary layer over finite membrane surfaces.

Although much effort has been expended and numerous papers have been published on the subject of boundary-layer stability over compliant surfaces, there is still much to learn and understand about this interesting subject. As reviewed above, the research has so far been focused only on the 2D temporal and spatial DNS of instability waves over surface-based membrane models. To our knowledge, the spatial evolution of unstable waves over finite viscoelastic layers, a case of some practical significance by virtue of their ease of construction, has yet to be modelled and studied. We consequently devote ourselves to its investigation in the present paper.

2. Governing equations and boundary conditions

Fig. 1 shows a schematic of the computational domain for the fluid–solid wave interaction problem. In this section, the governing equations and the boundary conditions for linear wave propagation in the fluid and solid layers are described. The interaction between the two domains is governed by the continuity of perturbation velocity and stresses across the domain interface, which are implemented in a linear manner.

2.1. Perturbation flow equations

Fasel [25] carried out the first accurate direct numerical simulation of Tollmien–Schlichting waves in Blasius boundary layer on a rigid surface. He employed the vorticity–velocity (ζ, u, v) formulation on a non-staggered grid. Giannattasio and Napolitano [26] pointed out such a formulation would require special treatment for the wall vorticity boundary condition in

order to attain second-order accurate divergence-free solution. Fasel [25], however, avoided the direct computation of vorticity values at the rigid wall by employing the equation $\partial\zeta/\partial x = -\partial^2 v/\partial y^2$ at the wall. It is not clear if this procedure can be formally justified, although it has provided acceptably good results in actual applications [20].

The vorticity–streamfunction (ζ, ψ) method, on the other hand, is widely used to study two-dimensional fluid flow because of its simplicity and the fact that the divergence-free condition could be satisfied automatically by the definition of the streamfunction. The wall vorticity ζ_w is computed via the distribution of ψ in the vicinity of the wall. Guj and Stella [27] and Napolitano and Pascazio [28] have shown that the second-order (ζ, ψ) formulation is equivalent to the (ζ, u, v) formulation on a staggered grid. However, the (ζ, ψ) formulation has the advantage over the latter in that it involves only two equations in two unknowns. For time-accurate evolution of flow, the vorticity and streamfunction fields should be solved simultaneously. This may be achieved by adopting a direct or an iterative time-implicit procedure. The vorticity–streamfunction formulation is chosen in our 2-D study of linear wave propagation here. The governing equations for the perturbation vorticity ζ and streamfunction ψ fields are:

$$\frac{\partial\zeta}{\partial t} + \frac{\partial}{\partial x}(u\zeta + \bar{u}\zeta + u\bar{\zeta}) + \frac{\partial}{\partial y}(v\zeta + \bar{v}\zeta + v\bar{\zeta}) = \frac{1}{Re}\left(\frac{\partial^2\zeta}{\partial x^2} + \frac{\partial^2\zeta}{\partial y^2}\right), \tag{1}$$

$$\frac{\partial^2\psi}{\partial x^2} + \frac{\partial^2\psi}{\partial y^2} = \zeta, \tag{2}$$

where

$$u = \frac{\partial\psi}{\partial y} \quad \text{and} \quad v = -\frac{\partial\psi}{\partial x} \tag{3a,b}$$

are the perturbation velocity fields. In the above equations, $\bar{u}$, $\bar{v}$, $\bar{\zeta}$ denote the velocity and vorticity fields of the unperturbed base flow. These are prescribed by the solution of the flat-plate boundary-layer equations. $Re = U^*_\infty \delta^*_0/\upsilon^*$ is the Reynolds number based on the free-stream velocity U^*_∞ of mean flow, the displacement thickness δ^*_0 at a suitable reference location, and the kinematic viscosity υ^*. Superscript asterisk denotes dimensional quantities.

Ribbon-excited waves are used in the present study for its greater fidelity with the typical experiments. The displacement thickness $\delta^*_0 = 1.7208\sqrt{\upsilon^* x^*_0/U^*_0}$ of the boundary layer at the location of the wall-mounted ribbon x^*_0 is chosen to be the reference length, where x^*_0 is measured from the leading edge of the flat plate. The non-dimensional distance x_0 (at ribbon location) is then given by $x_0 = (1.7208)^{-2} Re$. The non-dimensional stream coordinate x is then related to the local Reynolds number $Re_\delta = U^*_\infty \delta^*/\upsilon^*$ by

$$x = \frac{Re^2_\delta}{1.7208^2\, Re}. \tag{4}$$

2.2. Governing equations of viscoelastic solid layer

A viscoelastic layer with finite thickness (h) and finite length is placed along $x_{cs} \leqslant x \leqslant x_{ce}$ as shown in Fig. 1. The material of the solid layer is assumed to be elastic in dilatational deformation and Voigt-damped in deviatoric shearing. In the temporal domain, wave propagation in the layer obeys the following viscoelastic Navier's equations in non-dimensional form:

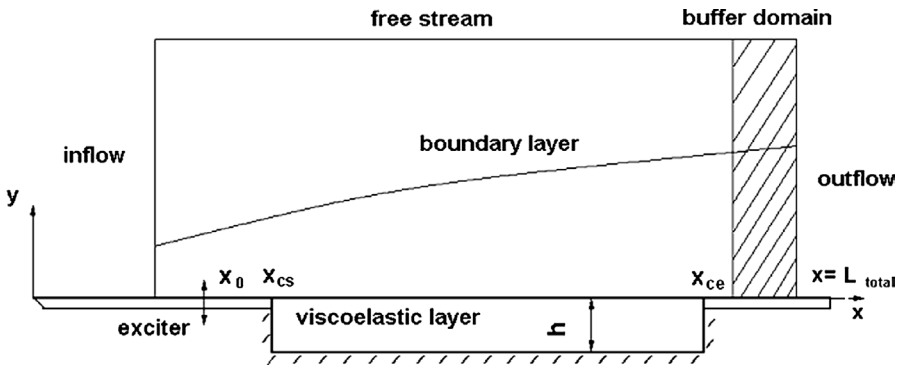

Fig. 1. Computational domain and buffer domain.

$$\rho_s \frac{\partial^2 \xi}{\partial t^2} = \frac{1}{2}\left(Y_{sr} + Y_{si}\frac{\partial}{\partial t}\right)\left(\frac{\partial^2 \xi}{\partial x^2} + \frac{\partial^2 \xi}{\partial y^2}\right) + \left(\frac{Y_v}{3} + \frac{Y_{sr}}{6} + \frac{Y_{si}}{6}\frac{\partial}{\partial t}\right)\left(\frac{\partial^2 \xi}{\partial x^2} + \frac{\partial^2 \eta}{\partial x \partial y}\right), \tag{5}$$

$$\rho_s \frac{\partial^2 \eta}{\partial t^2} = \frac{1}{2}\left(Y_{sr} + Y_{si}\frac{\partial}{\partial t}\right)\left(\frac{\partial^2 \eta}{\partial x^2} + \frac{\partial^2 \eta}{\partial y^2}\right) + \left(\frac{Y_v}{3} + \frac{Y_{sr}}{6} + \frac{Y_{si}}{6}\frac{\partial}{\partial t}\right)\left(\frac{\partial^2 \eta}{\partial y^2} + \frac{\partial^2 \xi}{\partial x \partial y}\right). \tag{6}$$

In the above equations, ξ and η are respectively the x-direction and y-direction displacement fields of the solid. ρ_s is the density of the solid layer. Y_v represents the elastic-dilatational modulus and is related to the more familiar bulk modulus K by $Y_v = 3K$. Y_{sr} is the elastic coefficient of the deviatoric modulus, which may be expressed in term of the elastic shear speed C_t by $Y_{sr} = 2\rho_s C_t^2$. The Y_{si}, on the other hand, is the viscous coefficient of the deviatoric modulus and can be calculated from $Y_{si} = 2d$, where d is the viscous damping coefficient of the material.

2.3. The coupling of perturbations in the flow and the solid layer

The perturbations in the flow and the solid layer are coupled by the requirements of velocity and stress continuity at the perturbed interface. For small-amplitude waves, the coupling conditions may be linearized about the mean flow-wall interface ($y = 0$). Velocity continuity yields the following interface coupling conditions between the perturbations of the flow and the viscoelastic layer at $y = 0$:

$$u_w = \frac{\partial \xi}{\partial t} - \eta \frac{\partial \bar{u}}{\partial y} \tag{7}$$

and

$$v_w = \frac{\partial \eta}{\partial t}. \tag{8}$$

The normal and shear stresses acting on the top surface of the viscoelastic layer due to flow perturbations are given by:

$$\sigma = -p_w + \frac{2}{Re}\left(\frac{\partial v}{\partial y}\right)_w, \tag{9}$$

$$\tau = \frac{1}{Re}\left(\frac{\partial u}{\partial y} + \frac{\partial v}{\partial x}\right)_w, \tag{10}$$

where p_w denotes the flow perturbation pressure at the mean flow-wall interface. These are matched to corresponding boundary stresses in the viscoelastic layer, which are given by

$$\sigma = Y_{sr}\frac{\partial \eta}{\partial y} + Y_{si}\frac{\partial}{\partial t}\left(\frac{\partial \eta}{\partial y}\right) + \frac{1}{3}(Y_v - Y_{sr})\left(\frac{\partial \xi}{\partial x} + \frac{\partial \eta}{\partial y}\right) - \frac{Y_{si}}{3}\frac{\partial}{\partial t}\left(\frac{\partial \xi}{\partial x} + \frac{\partial \eta}{\partial y}\right), \tag{11}$$

$$\tau = \frac{Y_{sr}}{2}\left(\frac{\partial \xi}{\partial y} + \frac{\partial \eta}{\partial x}\right) + \frac{Y_{si}}{2}\frac{\partial}{\partial t}\left(\frac{\partial \xi}{\partial y} + \frac{\partial \eta}{\partial x}\right), \tag{12}$$

at the mean interface. The flow perturbation pressure p_w is obtained here by integrating the y-direction perturbation Navier–Stokes equation from the free stream through the boundary layer to the mean interface:

$$p_w = \int_0^{\text{freestream}} \left[\frac{\partial v}{\partial t} + \frac{\partial(\bar{u}v + u\bar{v} + uv)}{\partial x} + \frac{\partial(2\bar{v}v + vv)}{\partial y} - \frac{1}{Re}\left(\frac{\partial^2 v}{\partial x^2} + \frac{\partial^2 v}{\partial y^2}\right)\right] \mathrm{d}y. \tag{13}$$

Finally, the boundary conditions for the perturbation vorticity and streamfunction of the flow at the mean interface are prescribed by:

$$\zeta|_w = \left(\frac{\partial^2 \psi}{\partial x^2} + \frac{\partial^2 \psi}{\partial y^2}\right)_w, \tag{14}$$

$$\psi|_w = \int (-v_w)\,\mathrm{d}x \tag{15}$$

and

$$\psi_y|_w = u_w. \tag{16}$$

2.4. Boundary conditions

Arising from the need to optimize computational resources, the computational domain for many spatial DNS studies of boundary layer frequently starts from the vicinity of the vibrating ribbon or disturbance strip, such as in Fasel and Konzelmann [29]. Where inflow boundary is specified downstream of the disturbance source, boundary condition which reflects the spectral content of the supposed disturbance may be applied from a synthesis of Orr–Sommerfeld solutions [20,30]. In our simulation, the (mono-frequency) TS waves are generated by a vibrating ribbon source situated at the wall downstream of the inflow boundary, and the disturbance quantities are set to

$$\psi = \psi_x = 0 \quad \text{and} \quad \zeta = 0 \tag{17}$$

along the inflow boundary itself. This treatment presumes there is no significant propagation of source perturbation upstream. Any error arising from this will be quite insignificant, however, since waves reflected from the inflow boundary will simply mirror the frequency content of the perturbation source.

Because the disturbance velocities u and v decay rather slowly in the wall-normal direction, a rather large domain would be required in this direction. In our numerical model, a coordinate transformation is applied in the wall-normal direction. The transformation sets the free-stream boundary far away from the wall. This ensures that any artificiality in the implementation of the free-stream boundary condition does not contaminate the solution near the wall. The following coordinate transformation is used,

$$x = x_C, \qquad y = y(y_C), \tag{18a, b}$$

where

$$y(y_C) = \frac{y_{\max}\gamma y_C}{y_{C\max}\gamma + y_{\max}(y_{C\max} - y_C)}. \tag{19}$$

Here $y_{\max}$ refers to the height of the flow domain in the physical coordinate y. The height of the flow domain in the transformed coordinate is $y_{C\max}$, while the γ is a real constant, which can be used to adjust the distribution of computational grid points in the physical coordinate y. We set

$$\psi(y_{\max}) = \psi_y(y_{\max}) = 0 \quad \text{and} \quad \zeta(y_{\max}) = 0, \tag{20}$$

where a value of $y_{\max} > 65$ is used.

The buffer domain technique of Liu and Liu [30] is further applied here for the vorticity–streamfunction formulation to reduce upstream reflection of waves from the outflow boundary. A schematic of the buffer domain is given in Fig. 1. Finally, the traditional extrapolation method is employed for ψ and ζ based on

$$\frac{\partial^2\psi}{\partial x^2} = 0 \quad \text{and} \quad \frac{\partial^2\zeta}{\partial x^2} = 0 \tag{21a, b}$$

along the outflow boundary of the buffer domain at $x = L_{\text{total}}$.

Perfect adhesion is assumed for the joins between the viscoelastic layer and the rigid plate. Zero displacement boundary conditions are thus applicable for all the three sides of the layer that are in contact with the plate:

$$\xi = 0, \quad \eta = 0 \quad \text{for } x = x_{\text{cs}}, \tag{22}$$

$$\xi = 0, \quad \eta = 0 \quad \text{for } x = x_{\text{ce}}, \tag{23}$$

$$\xi = 0, \quad \eta = 0 \quad \text{for } y = -h. \tag{24}$$

3. Numerical schemes

Many discretization schemes in space and time have been used by researchers to simulate boundary-layer transition. Transition simulations traditionally employ second-order implicit, or third- and fourth-order explicit temporal schemes. The data storage capacity of current computers, however, limits the extensive use of high-order explicit schemes when the spatial domain is large or when high spatial resolution is required. To conserve memory for spatial resolution and to increase the stability of our code, which is even more crucial for studying the interactions between transitional boundary-layer flow and compliant surfaces, the second-order backward Euler difference scheme is used for the time marching of the perturbation flow equations:

$$\frac{\partial\phi}{\partial t} = \frac{3\phi_t - 4\phi_{t-\Delta t} + \phi_{t-2\Delta t}}{2\Delta t} + \mathrm{O}(\Delta t^2). \tag{25}$$

Finite-difference methods and finite-difference/spectral methods have been the most popular discretization schemes for boundary-layer transition simulation. In the present work, the second-order central difference scheme is used for the discretization of the perturbation NS equations.

A uniform grid is employed for the solid layer in both coordinate directions. In the interior of the domain, fourth-order central difference scheme is used for spatial discretization. The employment of the higher-order spatial scheme improves the overall stability of the solver. Backward Euler scheme is employed for the discretization of the temporal terms.

For ease of comparison with the established results of Yeo [7], the parameters and materials properties of the viscoelastic layers are specified with respect to a fixed lengthscale L^*, which is defined implicitly via a wall Reynolds number $Re_{(\mathrm{L})} = U_\infty^* L^*/\upsilon^*$ set equal to the value of 2×10^4. These wall parameters are rescaled to the lengthscale δ_0^* (displacement thickness of the boundary layer at the location of the exciter) during computational simulation as follows, where only the affected quantities are listed:

$$h = \frac{h_{(\mathrm{L})} L^*}{\delta_0^*} = \frac{h_{(\mathrm{L})} Re_{(\mathrm{L})}}{Re} \tag{26}$$

and

$$Y_{\mathrm{si}} = \frac{Y_{\mathrm{si(L)}} L^*}{\delta_0^*} = \frac{Y_{\mathrm{si(L)}} Re_{(\mathrm{L})}}{Re}. \tag{27}$$

4. Computational results and discussions

In this section, we shall refer to locations/points along the plate by their non-dimensional stream coordinate x or their displacement-thickness based Reynolds number $Re_\delta = U_\infty^* \delta^*/\upsilon^*$. In particular, Re_{in} and Re_{out} denote the Reynolds numbers at the inflow and outflow boundaries respectively, while Re_{cs} and Re_{ce} are the Reynolds numbers at the leading and trailing edges of the compliant panel. The stream coordinate x is related to the Reynolds number Re_δ by Eq. (4). The non-linear terms in Eq. (1) have been retained during computation, but their contribution to the results is negligible because of the small wave amplitudes that are used in all the cases considered here.

4.1. Code validations

The benchmark cases for 2D Tollmien–Schlichting waves over a rigid wall in Fasel and Konzelmann's [29] are first repeated to validate and verify the accuracy of the perturbation Navier–Stokes solver. Fig. 2 shows excellent agreement between our results and those of Fasel and Konzelmann for selected points on the neutral stability curve.

Comparison with the results of Wiplier and Ehrenstein [21] (hereafter W & E for short) for Blasius boundary layer on a damped tensioned membrane is next considered. For this case, the membrane is located between $Re_{\mathrm{cs}} = 504.811$ and $Re_{\mathrm{ce}} =$

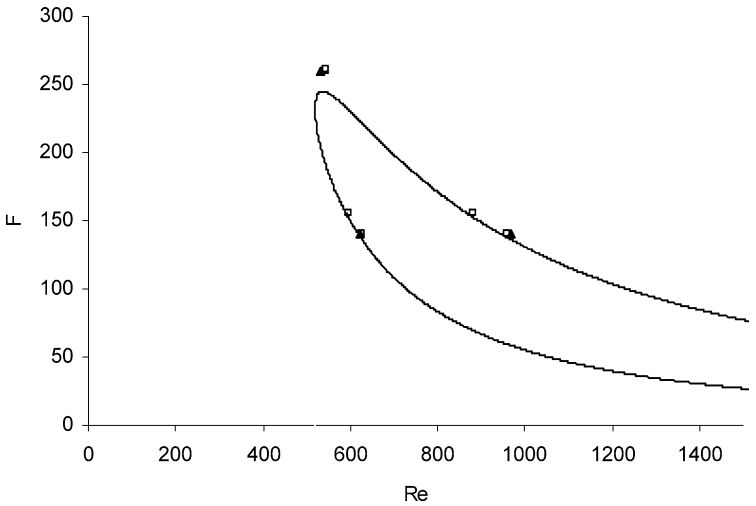

Fig. 2. Neutral stability points: — locally-parallel linear stability theory; □ present study based on inner maximum u; ▲ Fasel and Konzelmann [29] based on inner maximum u.

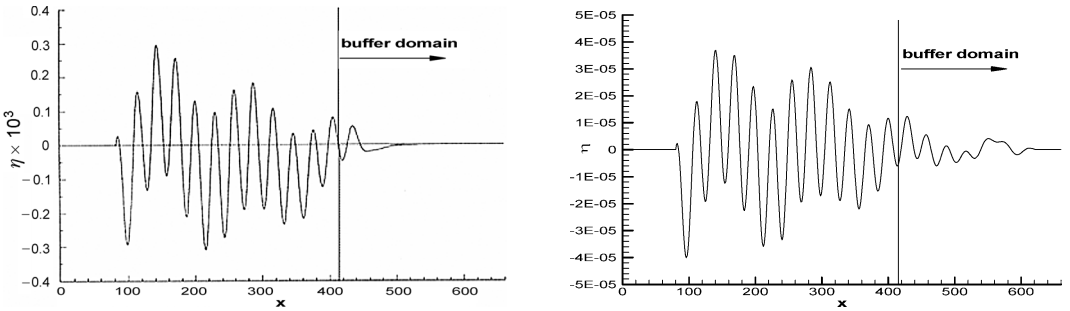

(a) (b)

Fig. 3. Surface displacement: (a) Fig. 11 in Wiplier and Ehrenstein [21] and (b) present study.

946.991. The properties of the membrane are as follows: $m_{(L)} = 0.0212$, $T_{(L)} = 15.0$, $d_{(L)} = 0.2$, $k_{(L)} = 0.0$, $Re_{(L)} = 580$ (here, m – mass, T – tension, d – damping and k – spring stiffness). The computational domain extends from $Re_{in} = 271.9$ to $Re_{out} = 974$, while the buffer domain begins from $Re_{buf} = 810$ over the membrane. Buffer functions are hence also applied to the membrane equations in the buffer region. The point-source perturbation is located at $Re = 400$ with a source frequency of $F = 218.9$ ($F = \omega_0/Re \times 10^6$) based on the displacement thickness at $Re = 400$. This is equivalent to the frequency $\omega_0 = 0.08756$ of the eigenfunction-based perturbation used by W & E along their inflow boundary at $Re = 400$. The computational grid is set at 401×71 with the vertical stretch parameter $\gamma = 1.8$ and 640 time steps per TS wave period is applied to maintain good temporal resolution. A small excitation amplitude ($\psi_A = 0.0001$) is adopted in our simulation. The simulation is carried out for 24 periods ($24T$) of the TS waves. The membrane displacement is compared against similar result of W & E in Fig. 3. The x-coordinate for the present result has been shifted to exactly match that of W & E for easier comparison. The surface displacement profile at $t = 24T$ bears a close similarity to that of W & E (Fig. 3). The wavelength of TS waves, as well as its modulation by co-existing surface wave mode(s), is almost identical with that of W & E. The maximum membrane displacement in W & E's result is about 0.03% of the reference displacement thickness (at $Re = 400$), which is about an order of magnitude larger than the present result. However, this is probably of minor significance as both waves are very much within the linear regime. This seems to be supported by the close similarity of the displacement profiles. The differences are really in the finer wave details, which may be due to a number of other factors. Firstly, the point excitation used in the present work may require a longer developing distance for it to achieve the same driving effect as the eigenfunction-based perturbation used by W & E. Secondly, the decay of the surface waves within the buffer domain is different, which reflects the use of different flow formulation and buffering strategy or parameters. Given that solids/solid surfaces are more strongly elliptic in space than uni-directional boundary layer flows at large Re, the behaviour of the membrane in the buffer region may be expected to have some influence on the upstream wave results. In the present work, we have tried not to damp the waves in the buffer zone too rapidly in order to minimize the upstream effects of buffering.

4.2. Periodic perturbations

In this section, six cases are performed to study the behaviour of ribbon-driven waves over viscoelastic layers. The solid and fluid parameters for these cases are tabulated in Table 1. The free-stream boundaries for these cases are all set to more than $65\delta_0$.

The neutral curves of linear stability or Orr–Sommerfeld theory (assumptions of infinite-length wall and locally-parallel flow) for these cases are shown in Figs. 4(a)–4(e). Cases 1 and 2 compares the propagation of TS waves over a compliant layer

Table 1
Solid and flow parameters of test cases

Case	Solid parameters ($Re_{(L)} = 20000$)					Flow parameters					
	$\rho_{(L)}$	$C_{t(L)}$	$d_{(L)}$	$K_{(L)}$	$h_{(L)}$	Re	Re_{in}	Re_{out}	Re_{cs}	Re_{ce}	F
1	1.0	1.0	0.0049	50	1.0	400	277.5	1035.9	428.1	990.0	180
2	1.0	1.0	0.0049	50	1.0	500	377.0	1198.6	529.3	1147.1	120
3	1.0	1.0	0.0049	50	0.6	400	277.5	1035.9	428.1	990.0	180
4	1.0	0.7	0.0049	50	1.0	400	277.5	1035.9	428.1	990.0	180
5	1.0	0.7	0.000098	50	1.0	400	277.5	1035.9	428.1	990.0	180
6	1.0	0.7	0.049	50	1.0	400	277.5	1035.9	428.1	990.0	180

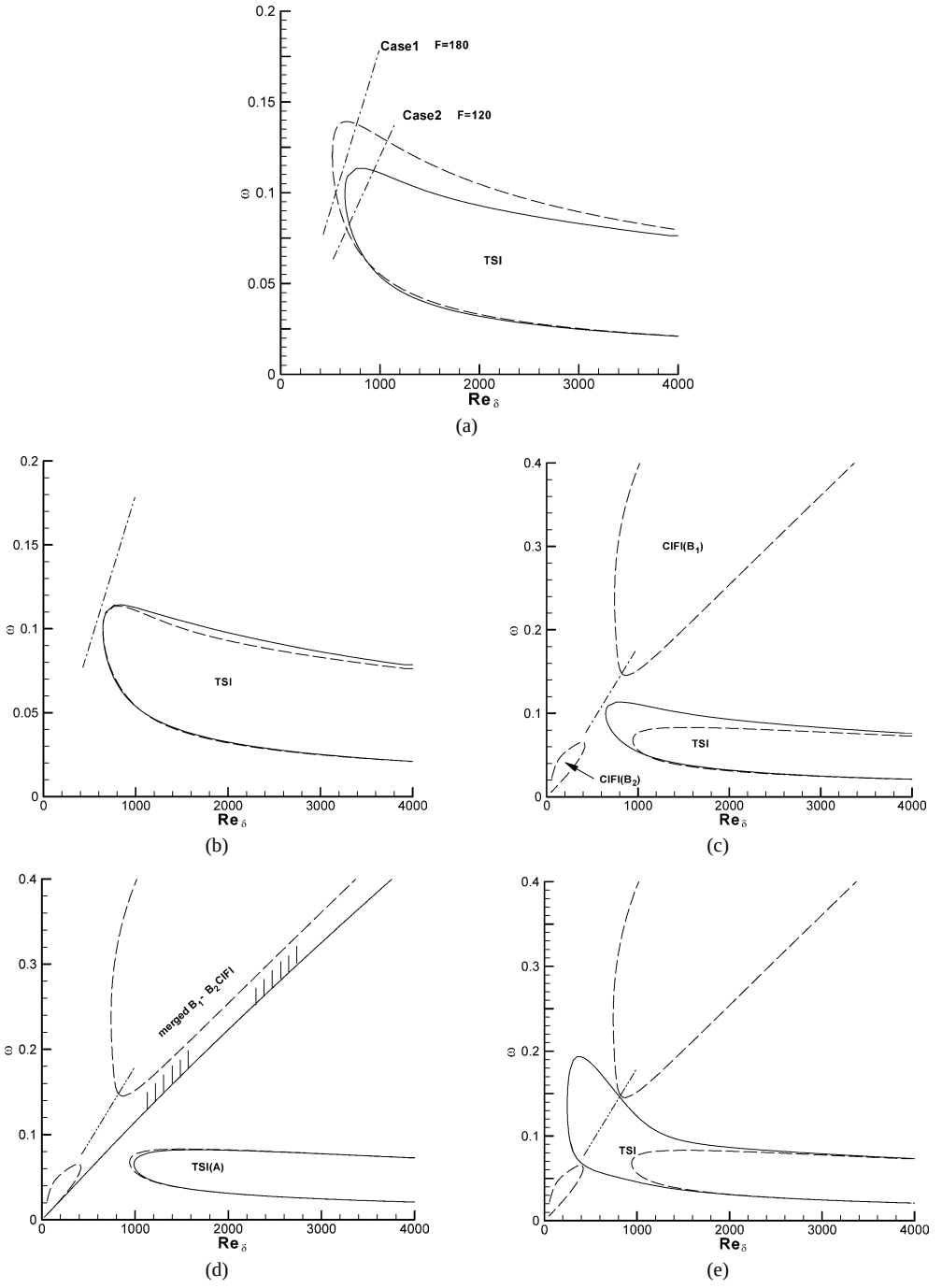

Fig. 4. Neutral curves for viscoelastic layers. (a) Comparison of Case 1, Case 2 (—) and rigid wall (- - -); (b) Comparison of Case 3 (—) and Case 1 (- - -); (c) Comparison of Case 4 (- - -) and Case 1 (—); (d) Comparison of Case 5 (—) and Case 4 (- - -); (e) Comparison of Case 6 (—) and Case 4 (- - -).

and the rigid wall. For these two cases, the compliant wall in question has been selected in accordance with linear stability theory to have no CIFI or wall-modes, see Fig. 4(a). Owing to the stabilizing effect of wall compliance on the TS waves, the compliant wall supports a reduced TS regime. The perturbation frequency for Case 1 has thus been selected such that the wave is unstable over a streamwise stretch of the rigid wall, but stays stable over the compliant layer. The Case 2 wave, on

the other hand, possesses unstable stretches over both the surfaces. Case 3 (Fig. 4(b)) is designed to show up the effects of layer thickness h, where a decrease in the thickness from Case 1 is seen to slightly reduce the unstable regime of linear TS waves. In Case 4, the shear stiffness $G = 0.5Y_{sr} = 0.5\rho C_t^2$ of the material is decreased (relative to wall of Case 1) leading to the occurrence of unstable CIFI or wall modes B_1 and B_2 (see Fig. 4(c)); where the CIFI (B_2) signifies the low-*Re* number branch, which is described in more details in Yeo [7]. The perturbation frequency is here selected to excite the CIFI waves. The wall damping in Case 4 is reduced drastically to near-zero level to give Case 5, where according to the linear stability theory, the unstable B_1- and B_2-CIFI regimes would be destabilized and merge to form a large CIFI regime (Fig. 4(d)). In Fig. 4(d), the barred pattern marks the unstable side of the CIFI neutral curve. The propagation of waves in this extended CIFI regime is considered. Finally, the application of material damping to suppress the CIFI or wall modes in considered by Case 6, which has ten times the level of material damping of Case 4. The CIFI would be completely suppressed according to linear stability theory (Fig. 4(e)). This is tested for finite viscoelastic panel by direct simulation here.

For all these cases, the computational mesh for the flow is set at 601×51, and for the solid layer 481×41. 640 time steps are again employed for each wave cycle to maintain temporal accuracy. Computation is typically carried out to 26 wave periods to allow for the full development of wave reflections from the trailing edge of the compliant layer. Several test runs are also performed to ensure that further increasing grid number does not significantly improve the results (i.e. checking of grid convergence).

4.2.1. Comparisons between viscoelastic layers and rigid wall

To compare the behaviour of TS waves over viscoelastic layers and a rigid wall, the compliant wall properties for Case 1 and Case 2 have been selected to ensure that the TSI modes are the dominant modes of instability on these walls, and that any co-existing CIFI modes would be comparatively weak. Case 1 is designed to let the 2D wave travel into a region where the TS waves would be amplified by the rigid wall and diminished by the compliant layer. The perturbation velocity u at $y = 1.05$ for Case 1 is plotted in Fig. 5(a) together with corresponding rigid wall results. Unlike the rigid wall results, the u-velocity perturbation over the solid layer in this figure decays almost monotonically as one would expect from its stability curve in Fig. 4(a). In this regard, the computational results do appear to agree qualitatively with the prediction of linear stability theory. In the absence of other unstable modes, it would appear that the slight non-monotonicity in decay might have been caused by interference with waves that are produced at the leading edge of the compliant layer. This recognizes the fact that the sharp discontinuity in the wall properties at the leading edge is able to act as a source for a wide spectrum of waves when suitably perturbed, in this case by the primary TS waves in the flow above. The excited wave would generally be a mode of the supporting medium, the flow-wall system, and may even be a damped mode deriving energy from the primary waves. The wave number spectrum in Fig. 5(b) shows clearly the presence of a small wave component in addition to the primary TS wave. We believe this wave mode, which is much weaker than the primary TS mode and possesses a much smaller wavenumber, is a wall-related or CIFI mode. The perturbation velocity u at wall surface ($y = 0$) in Fig. 5(c) is also supportive of the above observation. It shows clearly the decay of the primary TS waves, and its modulation by a longer wave mode. The wavenumber spectrum (Fig. 5(d)) of the u-velocity perturbation ($y = 0$) is also similar to that at $y = 1.05$, except that near to the wall, the second wave mode has grown in relative strength (though still significantly weaker than the primary TS wave). This is again symptomatic of a CIFI mode. Detailed comparison with the spectra of linear stability theory in Section 4.3 confirms the identity of this secondary wave as a CIFI or wall mode.

Fig. 6 shows the vertical displacement of the compliant surface for different times. A weak secondary (CIFI) wave, which travels ahead of the TS wave, can be observed in this figure. The relative wavelengths of the CIFI and the TSI waves are roughly consistent with the wavenumber peaks of Fig. 5(d). The primary TS wave reaches the trailing edge of the compliant layer before the completion of 16 wave periods. The propagation behaviour/history of the secondary (CIFI) mode indicates that it has been generated at the leading edge of the compliant panel. The important role of the leading edge in generating new wave modes has been highlighted before by Davies and Carpenter [20]. The temporal histories of the vertical displacement of the compliant surface at four different streamwise locations are presented in Fig. 7. Although the spatial patterns of wall displacements (Fig. 6) may be quite irregular in places, each point on the compliant surface attains temporal sinusoidal behaviour with its own constant amplitude after an initial transient phase. In other words, although there is more than one wave propagating over the compliant surface, they all share the same temporal frequency, which is the frequency of the ribbon source. The same temporal frequency is hence applicable at all points on the surface. It also shows that a steady periodic transient is eventually reached in less than 26 wave cycles of the computation. Fig. 8 shows the exaggerated displacement vector field inside the solid layer. Two types of 'rotational' structures may be discerned. The first one is much smaller in diameter and shallower in depth than the other. The second one is relatively larger and permeates almost the entire depth of the layer. Their relative sizes are compatible with the wavenumber peaks of the surface displacement in Fig. 5(d), and one may conclude that the smaller rotational structures are associated with the TS waves, while the larger ones with the CIFI waves.

In Case 2, the perturbation frequency is chosen such that the waves generated would be amplified by both the viscoelastic layer and the rigid wall. The perturbation velocity u at $y = 1.05$ is presented with the rigid wall results in Fig. 9(a). The results

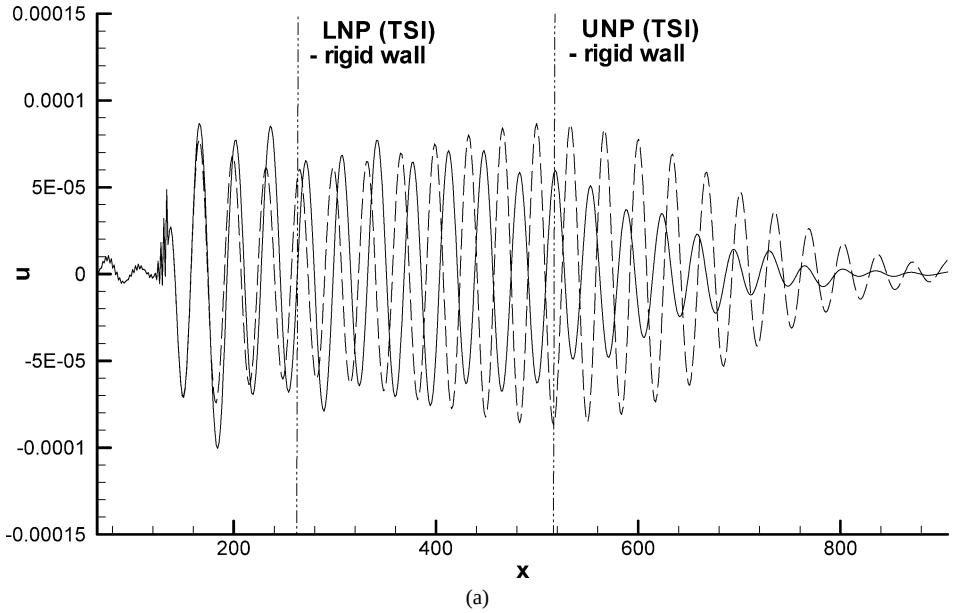

(a)

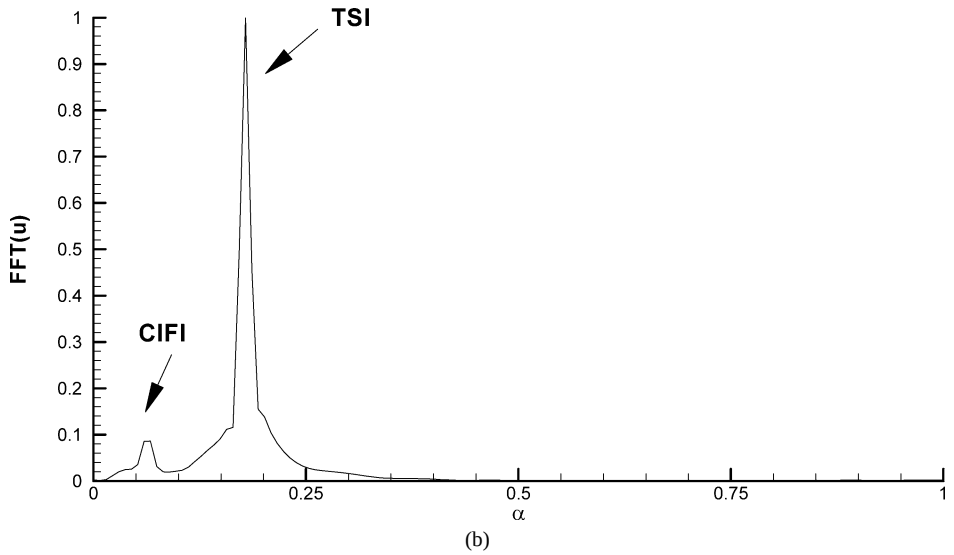

(b)

Fig. 5. (a) Perturbation velocity u at $y = 1.05$ for Case 1 (—) and rigid wall (- - -). (b) Wavenumber spectrum for u at $y = 1.05$ (Case 1).

show that the unstable region as well as the amplification rate of the TS wave is reduced considerably by this viscoelastic layer. This is consistent with the stability curves given for the layer and the rigid wall in Fig. 4(a). The wavenumber analysis in Fig. 9(b) for the u-velocity distribution shows that a weaker and longer CIFI wave is also present for this case. The perturbation velocity u at the compliant surface (Fig. 9(c)) and its wavenumber spectrum (Fig. 9(d)) demonstrate a consistent trend with Case 1 with regards to the enhanced presence of the CIFI modes at the wall.

4.2.2. Effect of thickness h

Case 3 is designed to study the consequence of reducing the thickness of the solid layer from that of Case 1. Owing to the relatively stiff nature of the materials used for these layers ($C_{t\,(\mathrm{L})} = 1$), the TS neutral curves for Cases 1 and 3 are closely similar (Fig. 4(b)). It is not surprising hence that there are only minor differences in their u-velocity distributions at $y = 1.05$ in the flow (Fig. 10(a)). At the wall (Fig. 10(c)), the differences are somewhat more pronounced, and one could see that the amplitude of the surface wave is reduced by the decreased thickness of the layer. The wavenumber spectra of the u-velocity fluctuations are given in Figs. 10(b) and 10(d). In each plot, the two most dominant peaks are coincident in terms of their

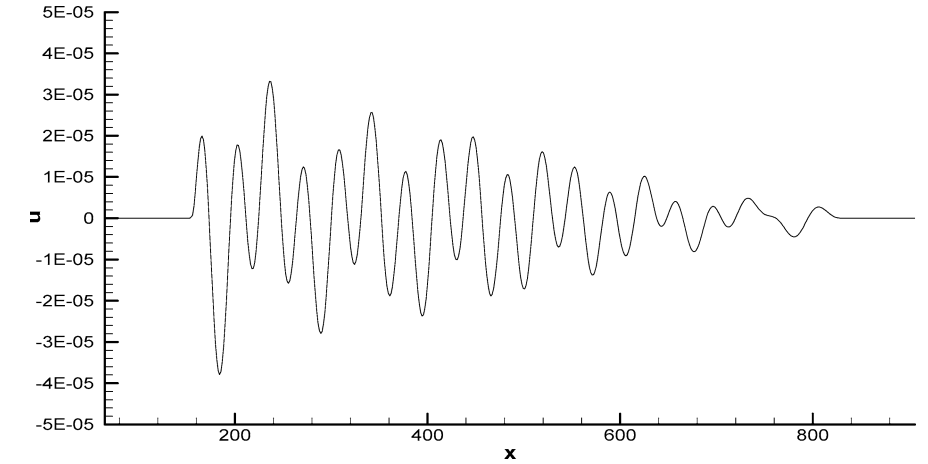

(c)

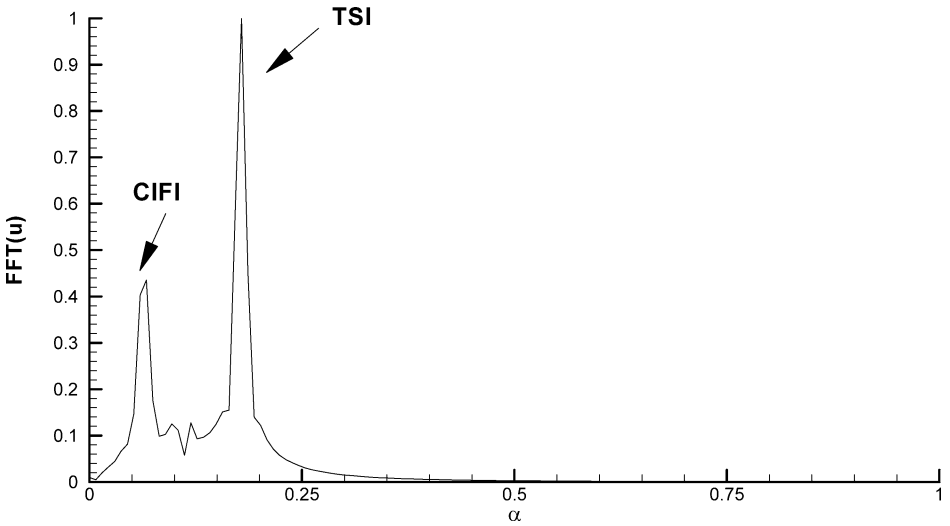

(d)

Fig. 5. (Continued). (c) Perturbation velocity u at $y = 0$ (Case 1). (d) Wavenumber spectrum for u at $y = 0$ (Case 1). Lower neutral point (LNP), upper neutral point (UNP).

wavenumber. Not unexpectedly, the lower peak, which corresponds to a damped wall-mode, is relatively more prominent at the wall than at $y = 1.05$. The wavelengths of the primary TS modes are nearly the same for both layers. The wavelength of the second mode is, however, significantly longer for the thinner layer (Case 3) than it is for Case 1 (Fig. 5(d)); showing the strong influence that wall parameters have on the CIFI mode.

4.2.3. Effect of elastic shear modulus Y_{sr}

The effect of the elastic shear modulus (material stiffness) on the unstable wave system is next considered. $C_{t\,(L)}$ is reduced from 1.0 in Case 1 to 0.7 in Case 4. The neutral curves for the two cases are compared in Fig. 4(c). Figs. 11(a) and 11(c) compare the u-velocity perturbations for the two cases at $y = 1.05$ and $y = 0.0$ respectively. The wave systems are quite different for the 2 cases. For Case 1, we have already witnessed a slowly decaying TSI mode that is consistent with the stability characteristics of the wall given in Fig. 4(a). For Case 4, Fig. 4(c) tells us that the wave perturbation will initially decay until a Reynolds number $Re \approx 830$ ($x \approx 580$). Beyond $x \approx 580$, we may expect to see a growing CIFI. Figs. 11(a) and 11(c) show a rapidly decaying TSI mode. The decaying TSI wave is clearly modulated by another mode of somewhat longer wavelength. An examination of the wavenumber spectra in Figs. 11(b) and 11(d) and comparison with similar spectra for Case 1 (Figs. 5(b) and 5(d)) indicates that the modulating wave is a CIFI; a decaying CIFI according to the stability curves in Fig. 4(c). For $x \geqslant 580$ to the end of the panel at $x \approx 827$, we expect to see a growing CIFI mode. This is not every obvious, however. We do not see clear sign of

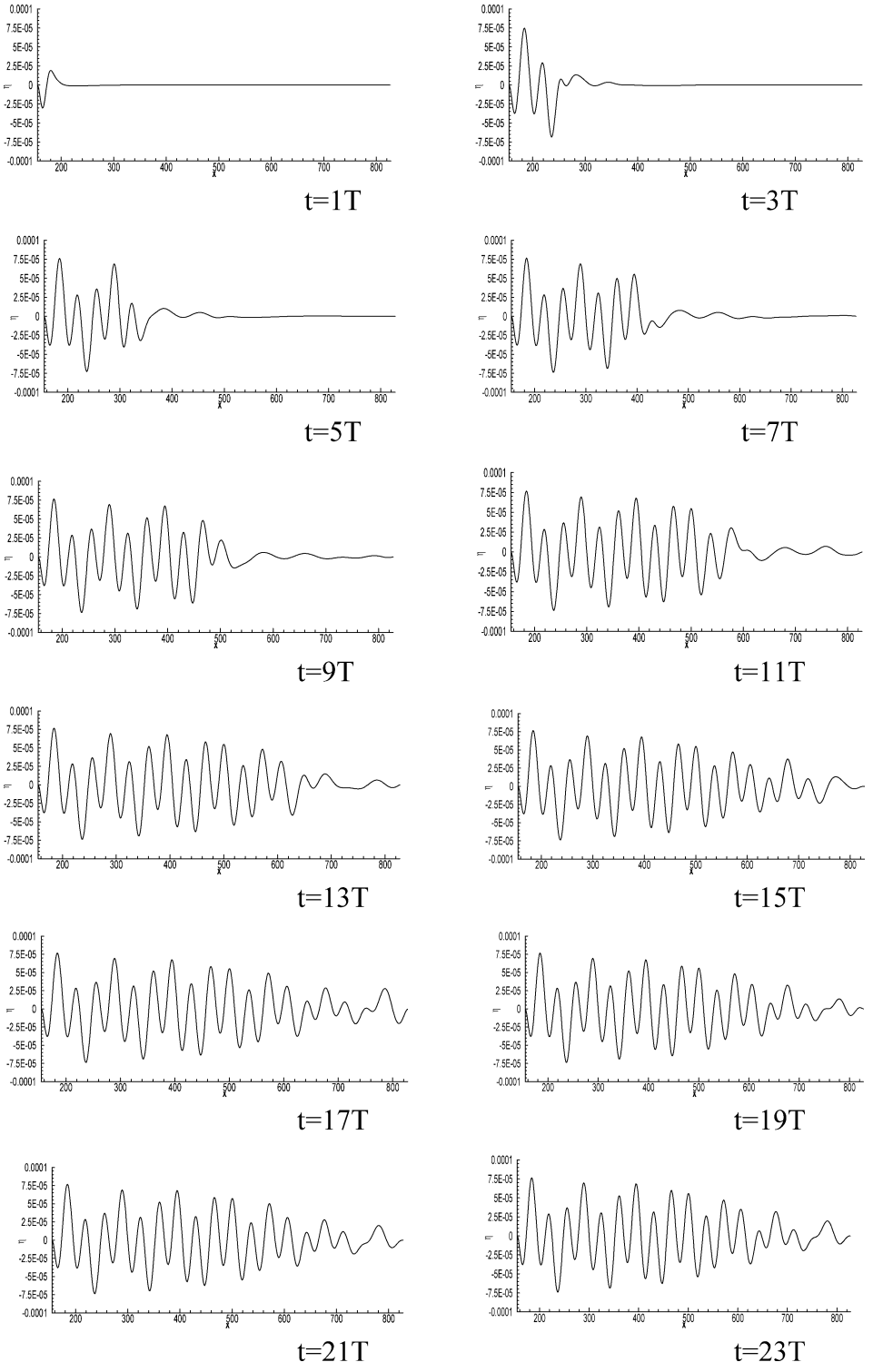

Fig. 6. Vertical displacement of compliant surface at different times (Case 1).

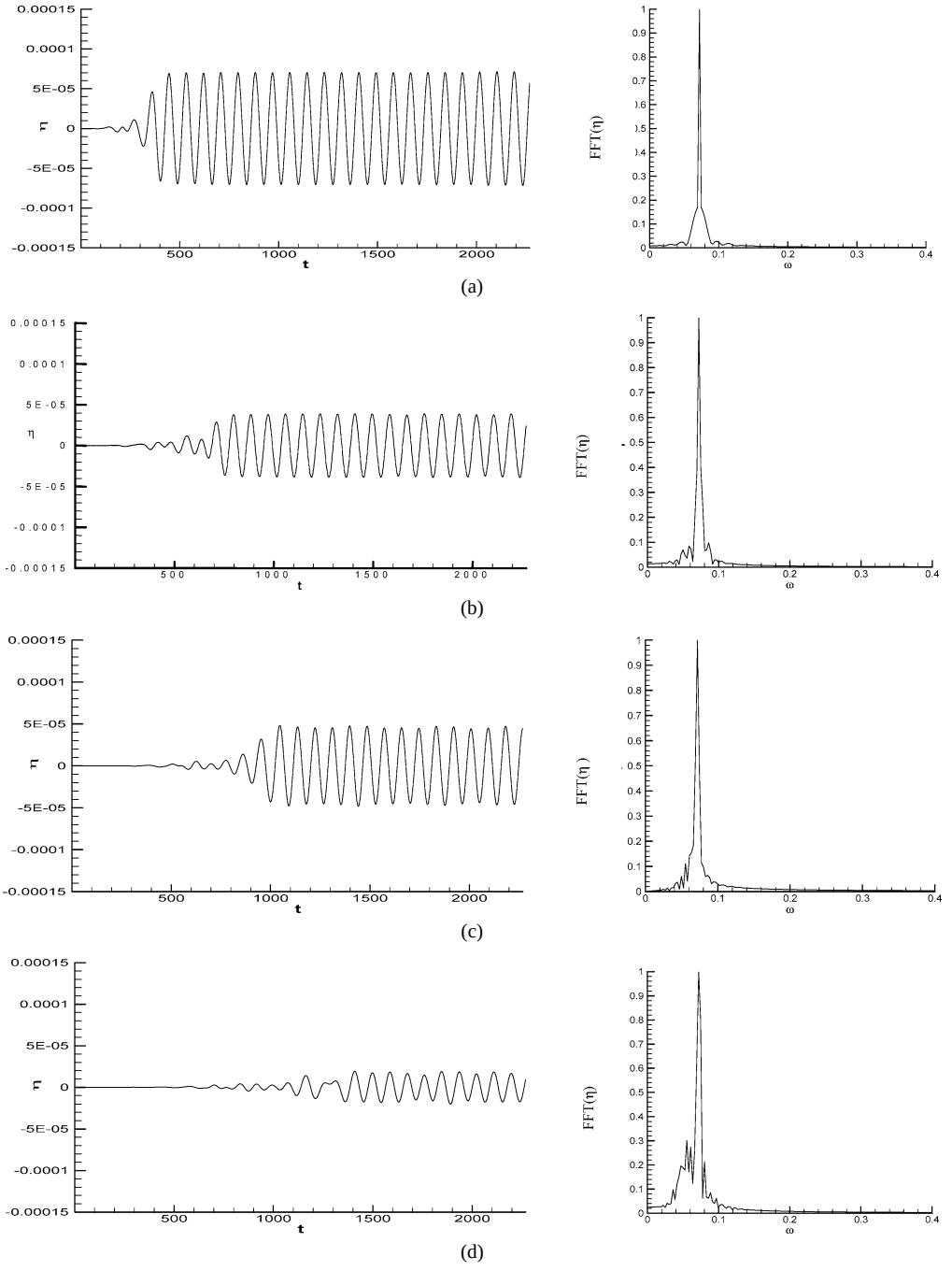

Fig. 7. History of vertical displacement and frequency spectrum at various points along the compliant surface for Case 1: (a) $x = 294.88$; (b) $x = 435.05$; (c) $x = 575.22$; (d) $x = 715.39$.

wave growth here, but instead merely a sustained wave. Further consideration shows that two factors may be responsible for this behaviour. Firstly, the amplification rate of the CIFI mode is very small over this region of the panel. Secondly, the short length of this segment of the panel due to the proximity of the panel's trailing edge (about 4 wavelengths of the perturbation wave) effectively limits any significant increase in the wave amplitude. Comparison of the wave spectra for Case 1 and Case 4 shows that the CIFI is clearly stronger in the latter case as well as possessing a shorter wavelength.

The comparative study of Case 1 and Case 4 demonstrates that reducing the material stiffness (Y_{sr}) may result in the destabilization of CIFI modes. Fig. 11(c) also reveals that the softer wall (Case 4) suffers significantly larger displacement on

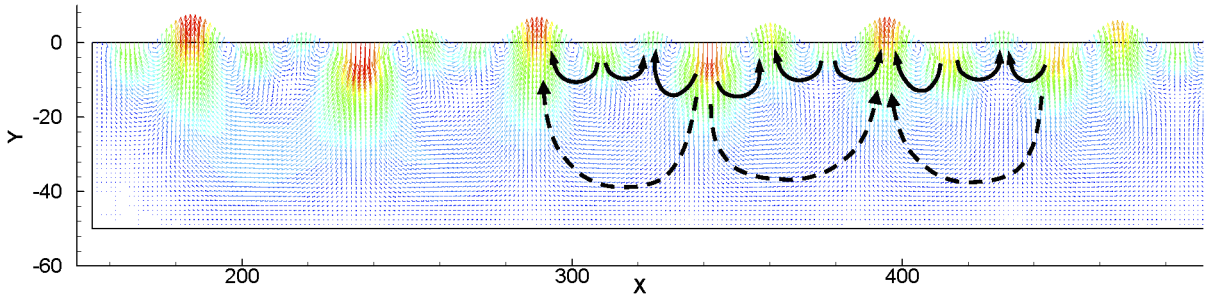

Fig. 8. Displacement vector field for viscoelastic layer of Case 1 (scale factor 1×10^5, colored by magnitude of displacement). Arrows indicate two types of counter rotating waves in the viscoelastic layer.

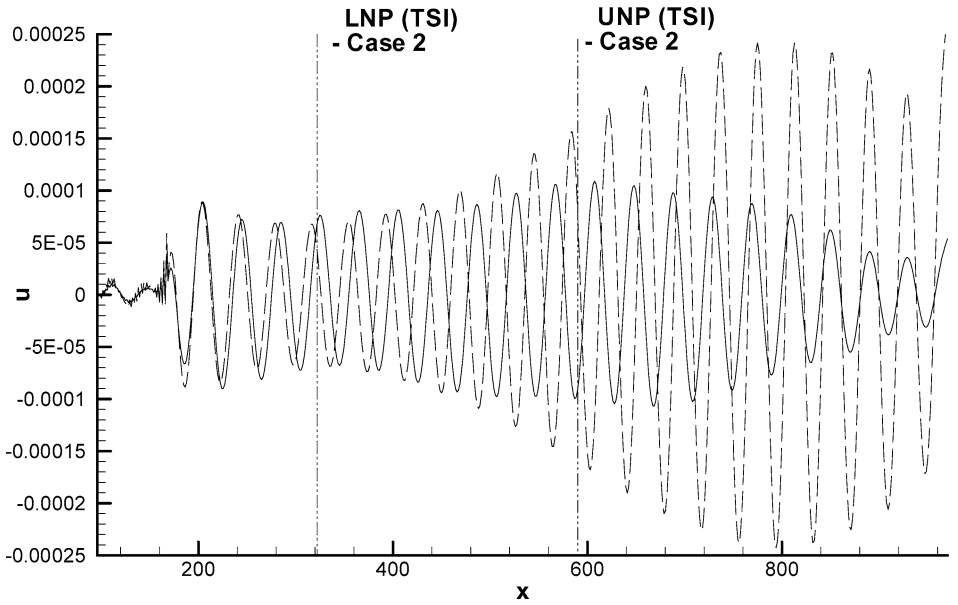

(a)

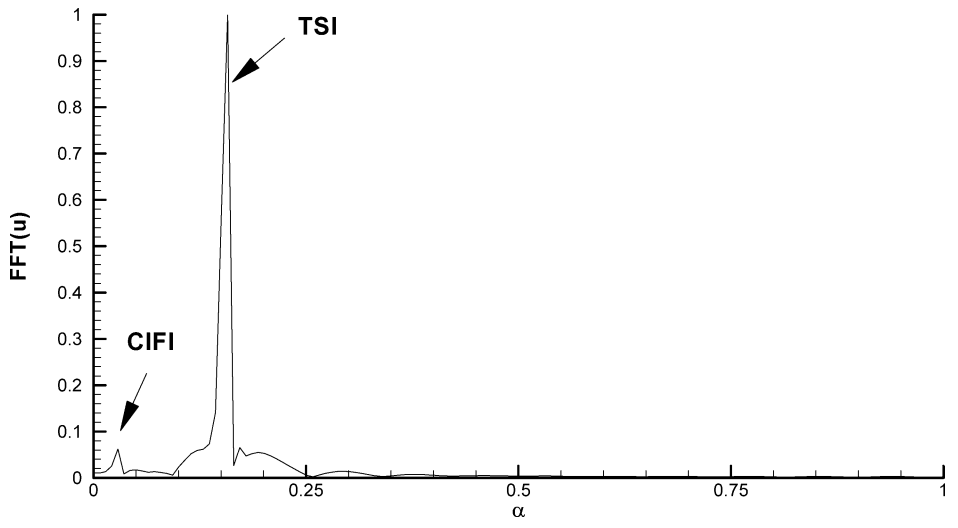

(b)

Fig. 9. (a) Perturbation velocity u at $y = 1.05$ for Case 2 (—) and rigid wall (- - -). (b) Wavenumber spectrum for u at $y = 1.05$ (Case 2).

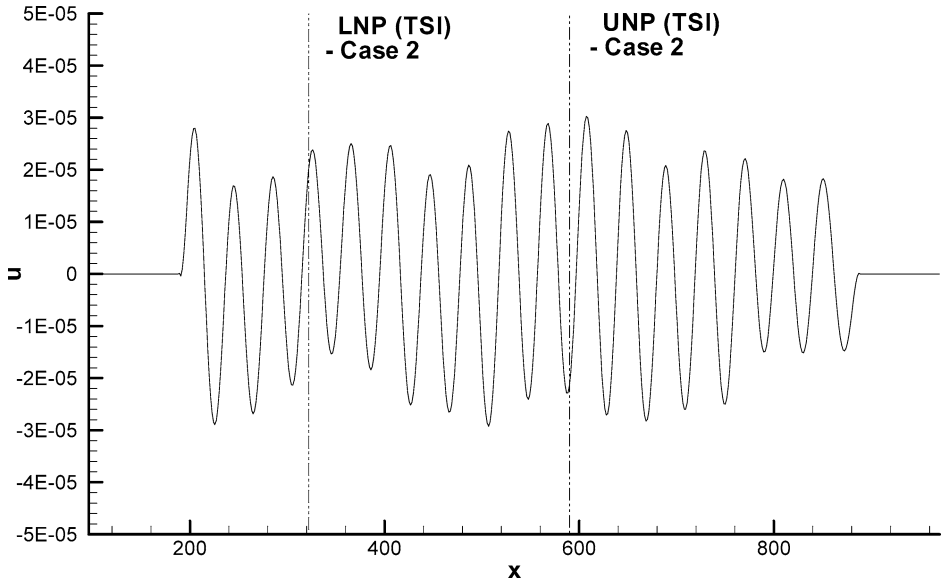

(c)

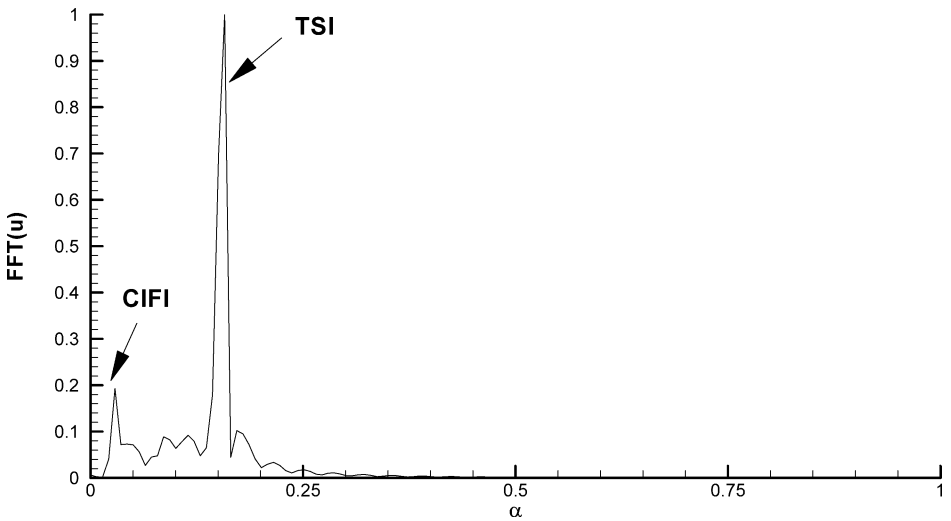

(d)

Fig. 9. (Continued). (c) Perturbation velocity u at $y = 0$ (Case 2). (d) Wavenumber spectrum for u at $y = 0$ (Case 2). Lower neutral point (LNP), upper neutral point (UNP).

its surface. This is not unexpected. More importantly though, we note that the perturbation wave in the flow (see Fig. 11(a)) grows rapidly over a few wave cycles as it travels past the leading edge of the compliant panel. Such leading edge amplification of waves is clearly undesirable and may be important where soft walls are concerned. This negative effect of the leading edge of finite panels was also noted by Davies and Carpenter [20] in their study of shear flow over membranes.

4.2.4. Effect of damping modulus Y_{si}

Case 5 features a layer that possesses a much lower level of material damping than Case 4. The comparison of their neutral stability curves in Fig. 4(d) shows that the CIFI is significantly destabilized by the reduction in the damping level, whereas the stability of the TS modes has improved slightly. Our direct numerical simulation results for Case 5 support this conclusion. The CIFI waves (see Figs. 12(a) and 12(c)), are now more clearly observed near the trailing edge of the compliant wall. They are also much more amplified compared with the waves in Case 4. On the other hand, near the leading edge where the TS waves are more dominant, the wave for Case 5 decays slightly faster compared with the same wave for Case 4 (see Fig. 12(c)).

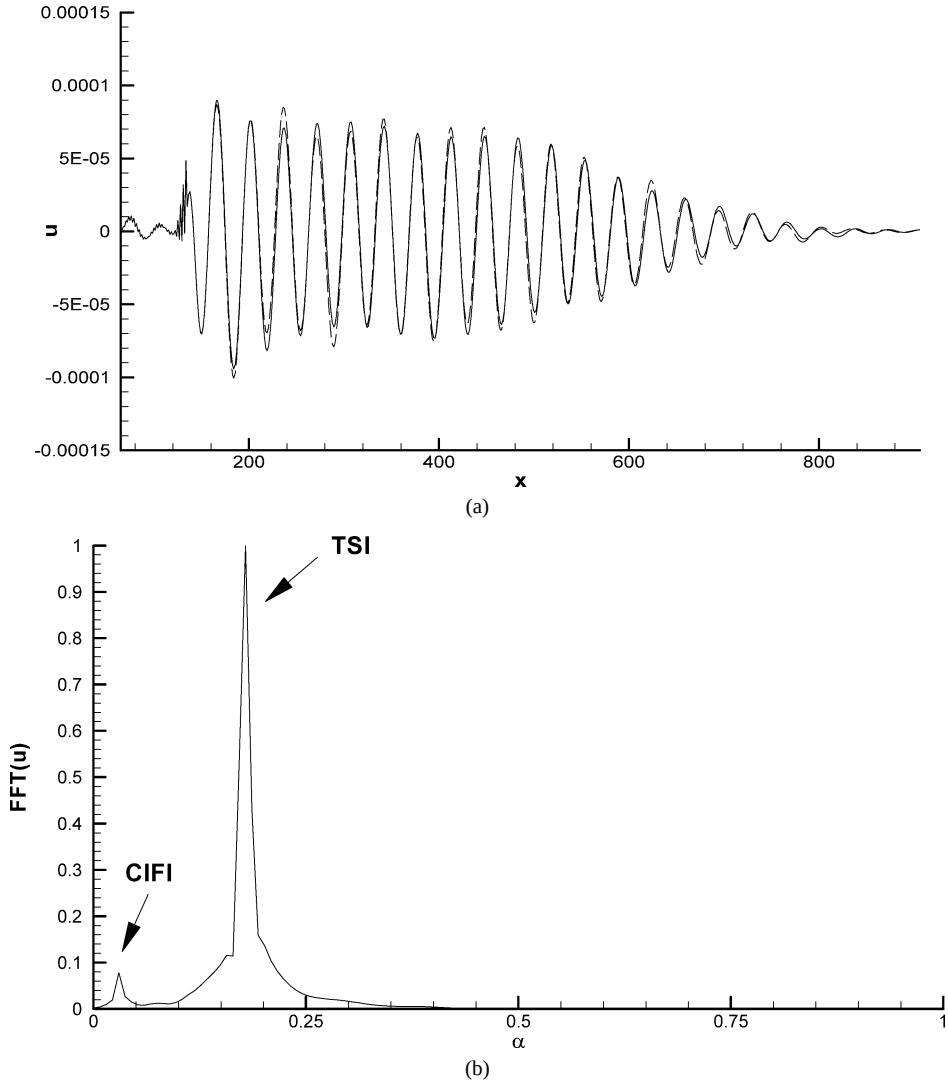

Fig. 10. (a) Perturbation velocity u at $y = 1.05$ for Case 3 (—) and Case l (- - -). (b) Wavenumber spectrum for u at $y = 1.05$ (Case 3).

The comparison between the wavenumber spectra also indicates that the CIFI for Case 5 (Figs. 12(b) and 12(d)) is much more prominent than the same for Case 4 (Figs. 11(b) and 11(d)). In Fig. 12(d), the CIFI mode has in fact become the dominant mode.

In Case 6, the material damping coefficient is increased to ten times its value in Case 4. Fig. 4(e) shows that at this high level of material damping, the CIFI are largely suppressed, leaving the TSI as the dominating mode. In fact, we expect the high damping to considerably destabilize and enhance the TS waves present in Case 4. This is clearly evident in Fig. 4(e), although the destabilizing effect on the TSI of Case 4 would be relatively mild at the lower frequencies. Fig. 13(a) compares the u-velocity distributions for Cases 6 and 4 at $y = 1.05$. Strong amplification of the wave may be seen in the first two-thirds of the wall, to be followed by monotonic decline in the remaining third. The rapid spatial growth of the TS waves is in-line with its strong destabilization by high damping at this frequency. The location of maximum amplitude ($x \approx 550$) in Figs. 13(a) and 13(c) corresponds approximately with the end of the amplification zone or the location of the upper neutral branch of the TSI ($Re \approx 810$) in Fig. 4(e) (more details in Section 4.4). The almost complete suppression of the CIFI, a rare occurrence so far, is also confirmed by the wavenumber spectrum in Fig. 13(b), which shows only a single dominating peak at the mean wavenumber of the TS mode with only a minuscule hint of other waves. This near monochromatic behaviour is naturally also reflected in the highly regular waveform of the TS waves given in the preceding figures. In general, CIFI and edge-related waves tend to show up more strongly at the wall. In the present case, these secondary waves are also singularly absent (see Figs. 13(a)

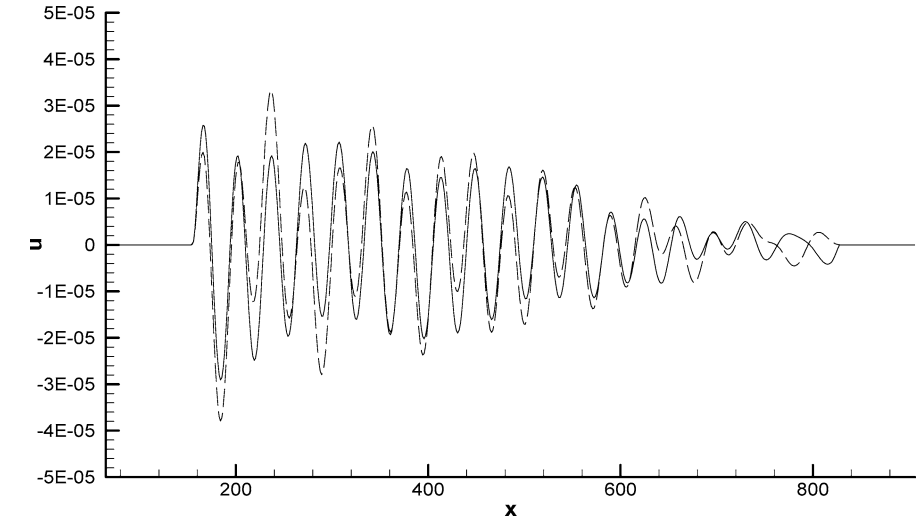

(c)

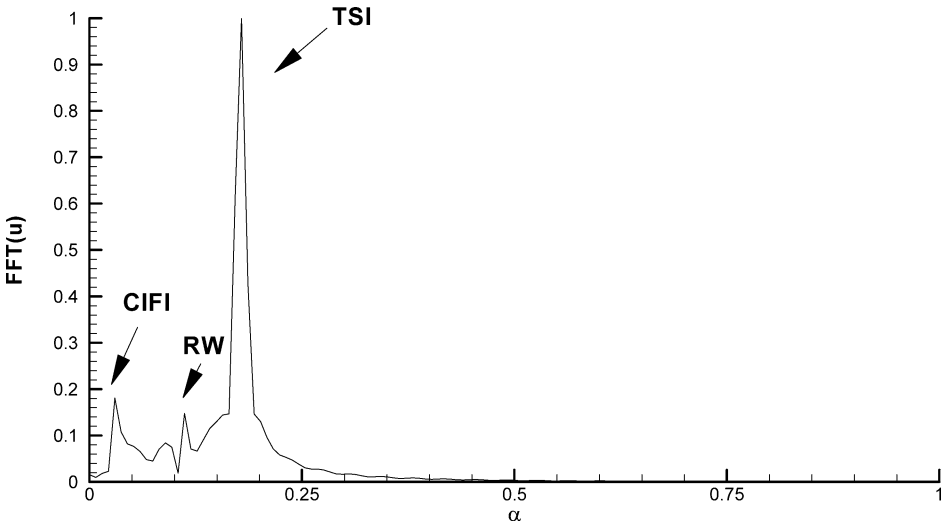

(d)

Fig. 10. (Continued). (c) Perturbation velocity u at $y = 0$ for Case 3 (—) and Case l (- - -). (d) Wavenumber spectrum for u at $y = 0$ (Case 3).

and 13(c)). This shows that the high level of material damping has indeed been effective not only in eliminating the CIFI but also in suppressing extraneous generation and reflection of waves from the leading and trailing edges of the compliant layer.

4.3. Comparisons between wavenumber spectra and eigenvalues

When TSI and CIFI modes are simultaneously present over a compliant surface, the combined wave may display complex variations of local wavenumber and amplification rate. This is further exacerbated by the inhomogeneous effects of boundary-layer growth and edge conditions, which produce spatial variation for each of the wave modes. It is thus difficult to decompose the combined wave system to determine in a precise manner the individual response of the constituent wave modes. Nevertheless, Fourier transform analyses would still shed considerable light on the behaviour of the individual waves that may allow us to compare the characteristics of these waves with results from linear stability analysis.

In this section, the wavenumber spectra for each of the preceding cases are compared with eigenvalues predicted by linear stability theory and tabulated in Table 2. The abbreviation RW is used to denote waves that are found from numerical simulation that cannot be accounted for among the TS and CIFI wave modes that we have found from our linear analyses. These are probably waves that are generated due to finite edge effects or else waves that were simply not captured in our linear analyses.

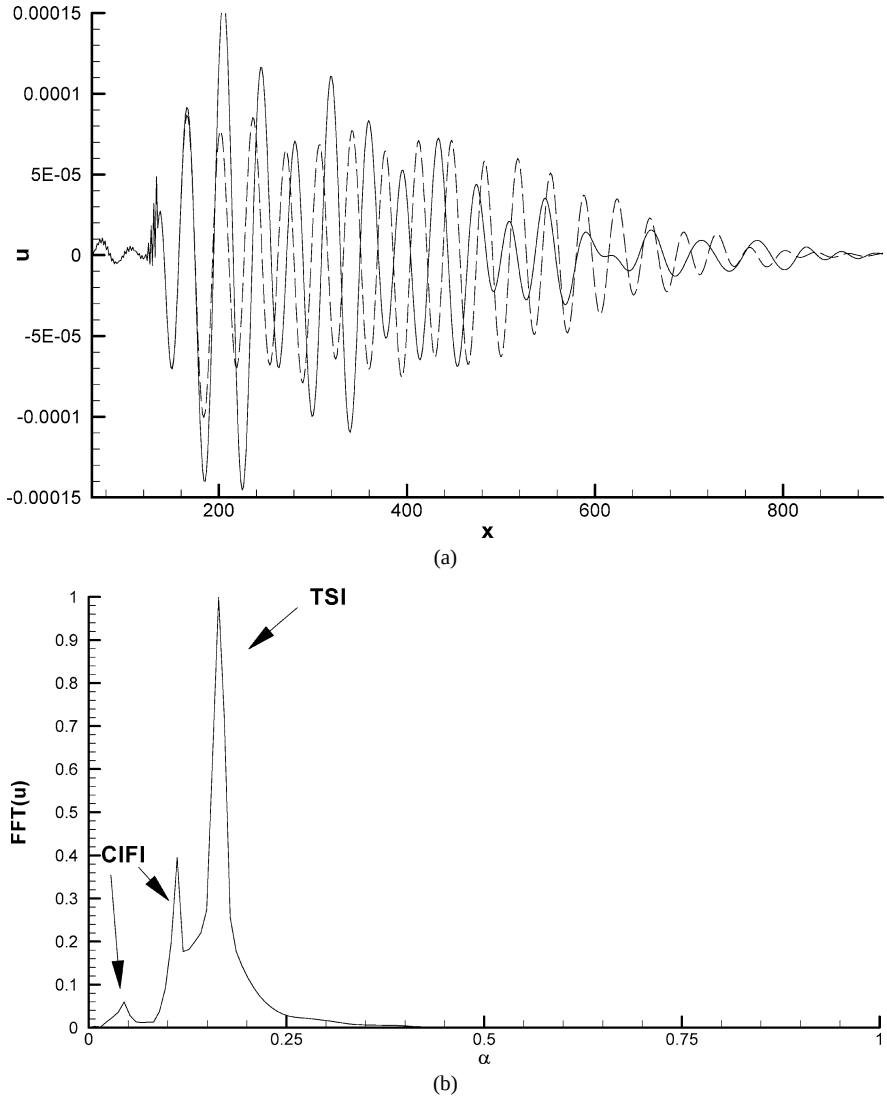

Fig. 11. (a) Perturbation velocity u at $y = 1.05$ for Case 4 (—) and Case l (- - -). (b) Wavenumber spectrum for u at $y = 1.05$ (Case 4).

RW thus stands for 'reflected' or 'remaining' waves. In the current comparison, the wavenumbers from numerical simulation are obtained from FFT analysis, while corresponding eigenvalues are calculated from linear stability theory applied at the location of the exciting source. From experience, it is noted that the local wavenumber of the instability waves (based on a fixed lengthscale) is only slightly altered in the course of their propagation downstream (this is also evident in the spatial wave results presented so far). This fact makes the comparison of the wavenumber spectra and linear stability predictions meaningful.

Table 2 shows that the wavenumbers of TSI modes obtained from the numerical simulations are in very good overall agreement with the predictions of linear stability theory in all cases. This further reinforces the validity of the current numerical investigation. Although there are no unstable regions of CIFI for Cases 1–3 in Figs. 4(a) and 4(b), damped or stable CIFI modes could still be detected in the present numerical simulation results. For Case 3, the computed wavenumber of the CIFI (B_1) mode is quite close to the theoretical eigenvalue. However, an additional, albeit small, wavenumber peak may also be detected in the u-velocity spectrum at $y = 0$ (Fig. 10(d)), which is apparently absent in the flow above the wall at $y = 1.05$ (Fig. 10(b)). It is suspected that this wavenumber peak might have been caused by waves generated or reflected from an edge of the finite compliant layer, or merely a mode that is not captured in our normal-mode analysis. There are two spectra peaks for CIFI modes for each of Cases 4 and 5. The larger peaks agree very well with linear stability predictions. The wavenumbers α_r for the smaller spectra peaks at $y = 1.05$ (Figs. 11(b) and 12(b)) also agree surprisingly well with linear stability predictions (Table 2). However, the corresponding α_r values of the peaks at the wall ($y = 0$) in Figs. 11(d) and 12(d) deviate somewhat from the

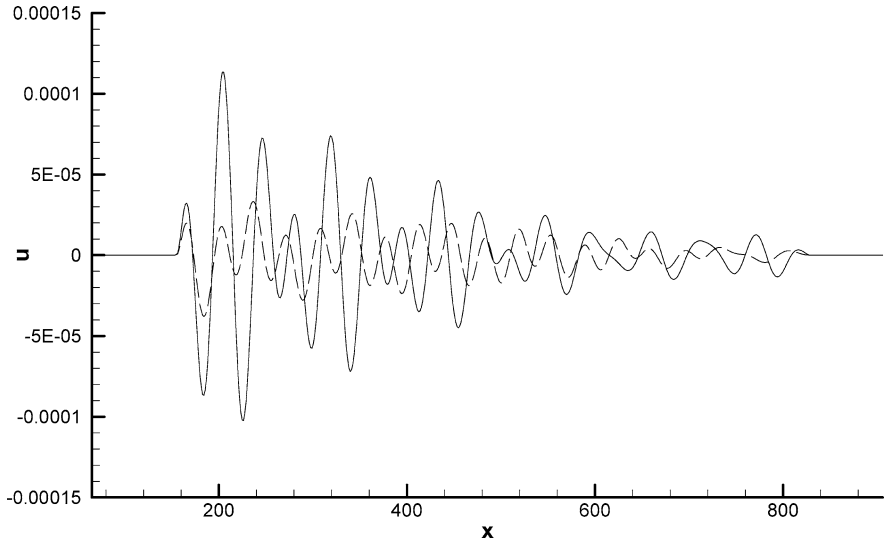

(c)

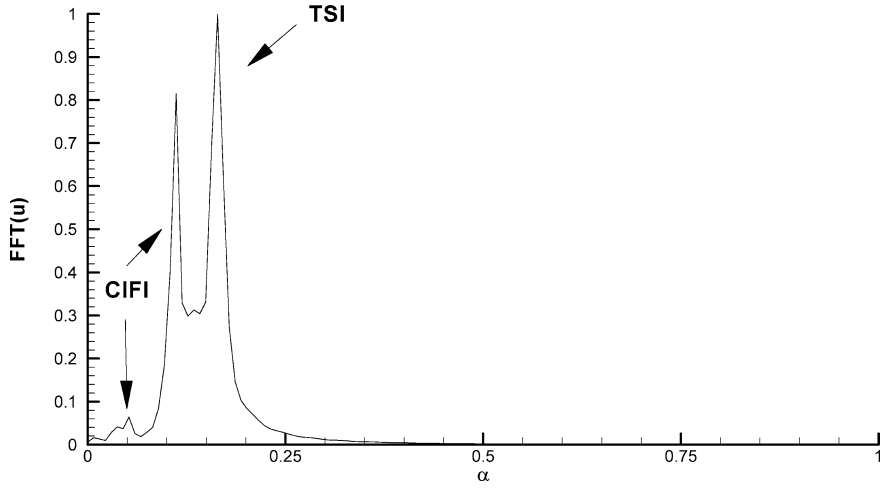

(d)

Fig. 11. (Continued). (c) Perturbation velocity u at $y = 0$ for Case 4 (—) and Case 1 (- - -). (d) Wavenumber spectrum for u at $y = 0$ (Case 4).

Table 2
Comparisons of wavenumber spectra and eigenvalues

Case	Wave number from FFT of numerical results				Real part of eigenvalues α from linear stability theory			
	TSI	CIFI		RW	TSI	CIFI		RW
1	0.180	0.065	–	–	0.1827	0.0628	–	–
2	0.154	0.032	–	–	0.1604	0.0303	–	–
3	0.180	0.032	–	0.110	0.1827	0.0327	–	?
4	0.164	0.111	0.044*	?	0.1650	0.1100	0.04607	?
			0.051†					
5	0.164	0.113	0.047*	0.133	0.1652	0.1092	0.04605	?
			0.051†					
6	0.167	–	–	–	0.1713	–	–	–

* At $y = 1.05$.
† At $y = 0$.

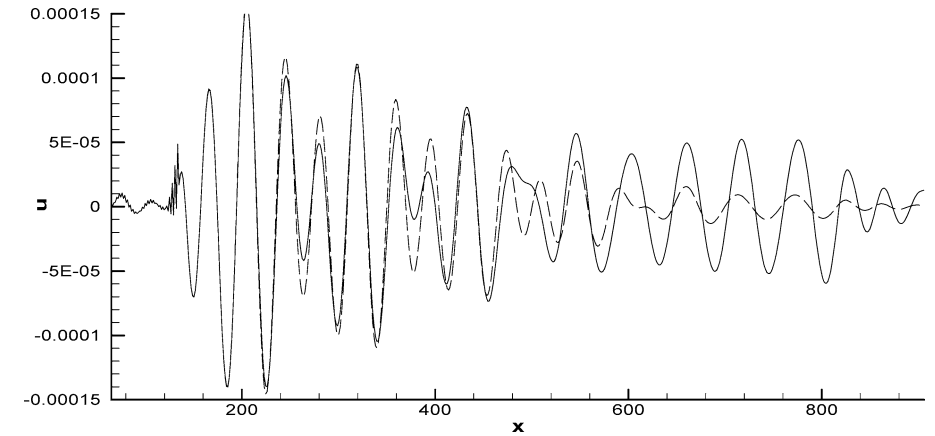

(a)

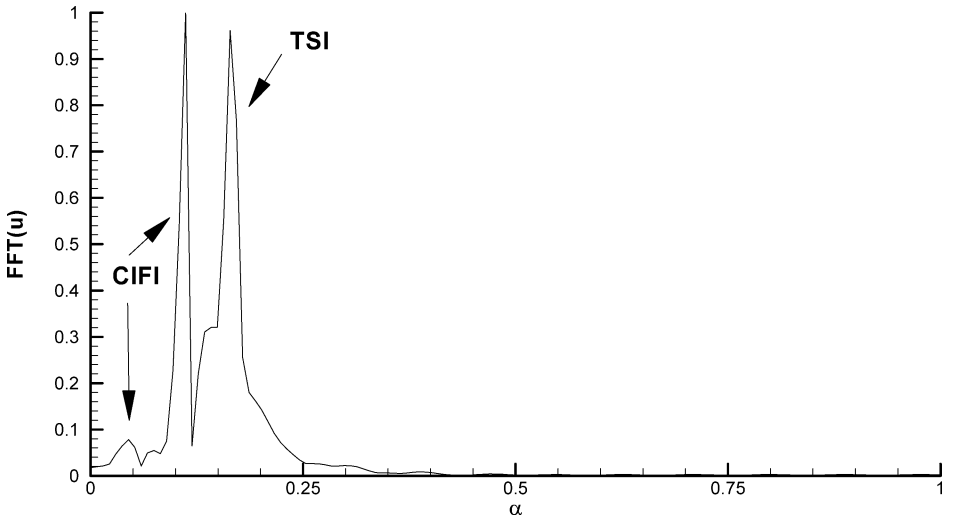

(b)

Fig. 12. (a) Perturbation velocity u at $y = 1.05$ for Case 5 (—) and Case 4 (- - -). (b) Wavenumber spectrum for u at $y = 1.05$ (Case 5).

theoretical values. More careful examination shows that these modes appear to be mingled with other long-wave modes that may have developed due to the presence of panel edges.

4.4. Non-parallel effects on TSI

The amplitude of the perturbation velocity u along the wall at different heights y for Case 2 is plotted in Fig. 14 with corresponding results of locally-parallel linear stability theory. The amplitude at a given point is determined by recording the maximum absolute value of the perturbation quantity over time after a state of steady periodic transient has been attained. Corresponding amplitude curves based on other perturbation quantities such as maximum $|u|$ and maximum $|v|$ etc. are also given in Fig. 15. A prominent feature of the results is the oscillatory character of the amplitude curves. Our analysis shows that the oscillation is due to the presence of the co-existing CIFI, which cannot be effectively separated or decomposed from the TSI. The interference between the waves results in an oscillation, with a wavenumber equal to the *wavenumber difference* ($\Delta\alpha$) of the two waves, being superposed on the overall trend of the amplitude curve. The wavenumber data for Case 2 in Table 2 yields a $\Delta\alpha \approx 0.122$, which would give a wavelength of 51.5 units or about 13.5 oscillations over the length of the compliant panel, extending from $x_{cs} = 189.2$ ($Re = 529.3$) to $x_{ce} = 888.7$ ($Re = 1147.1$). This is indeed the number of oscillations that one would deduce from Fig. 14, taking into account the missing wave segments at the two ends of the plot range. Additional small oscillations may be observed in the amplitude curve at $y = 0$ towards the downstream half of the compliant panel. This shows the presence of surface wave reflection from the trailing edge.

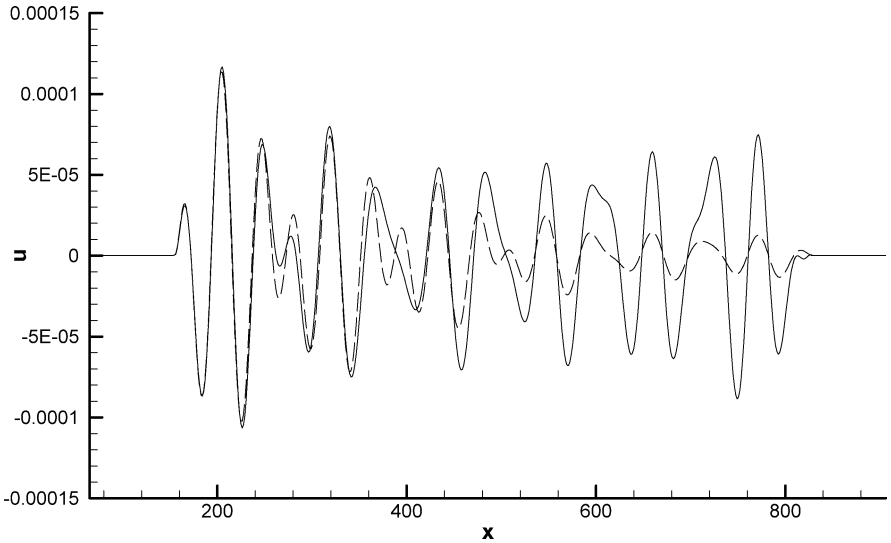

(c)

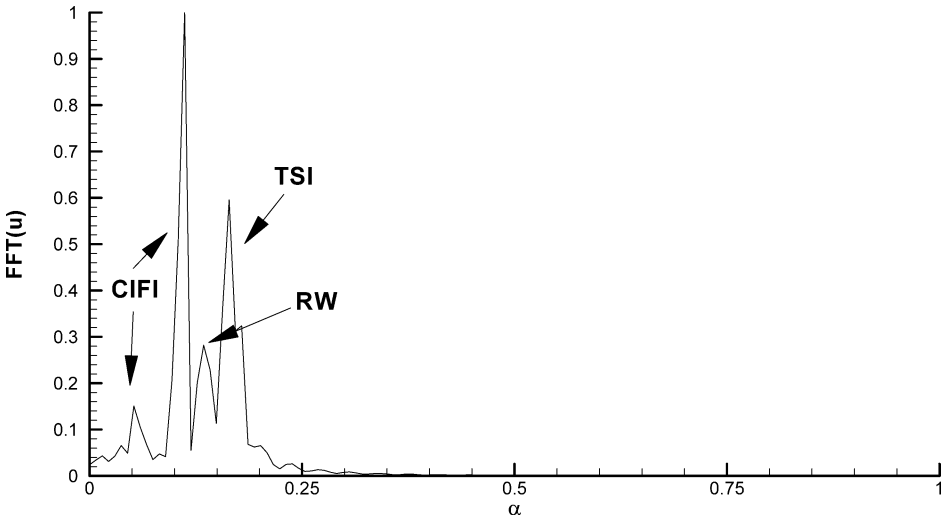

(d)

Fig. 12. (Continued). (c) Perturbation velocity u at $y = 0$ for Case 5 (—) and Case 4 (- - -). (d) Wavenumber spectrum for u at $y = 0$ (Case 5).

The presence of the oscillations makes it difficult for us to establish the precise position of the neutral stability points. Notwithstanding, visual estimates based on the mean interpolants of amplitude curves generally shows a small shift of the lower neutral points to lower Reynolds number and a larger shift of the upper neutral points to higher Reynolds number relative to the neutral points of locally-parallel linear stability theory. This appears to be also the general case for the lower and upper bound envelopes of the oscillatory amplitude curves. The differing positions of the neutral points for the different amplitude curves are a general reflection of the presence of the non-parallel effects of the boundary layer. The shift of the neutral points relative to the locally-parallel results to form an extended unstable region indicates that the non-parallel effects are generally destablizing on the TSI mode. This is consistent with the observation of Yeo, Khoo and Chong [10], based on a perturbation analysis.

Case 6 is an exceptional case in which high damping has effectively snuffed out most traces of CIFI leaving behind a well-defined TS wave. The amplification rate ($A^{-1}\,\mathrm{d}A/\mathrm{d}x$) curves for different measures of wave amplitude, including the normalized kinetic energy (an integral measure), are given in Fig. 16. The upper neutral points can be obtained easily for these amplitude measures. They all show a higher Reynolds number than the locally-parallel result, which again points to the destabilizing influence of boundary-layer non-parallelism. The lower neutral points could not be obtained because the upstream

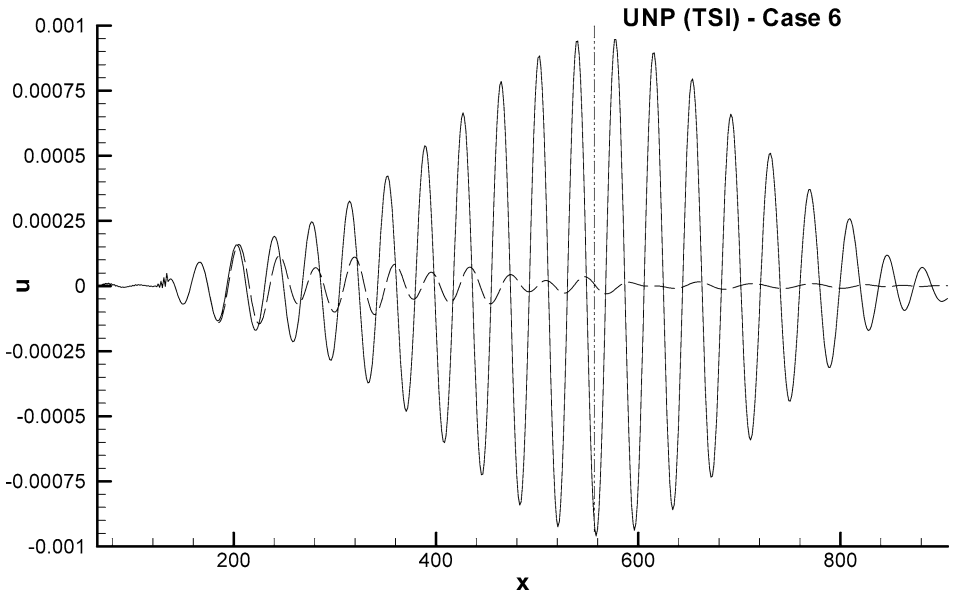

(a)

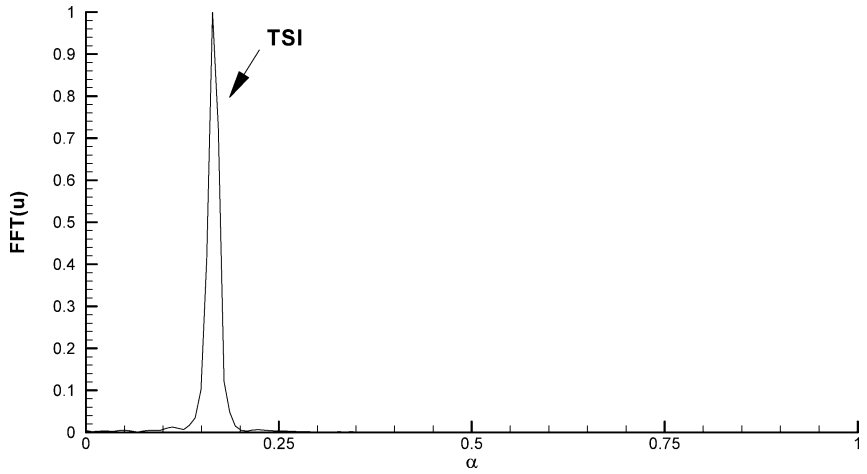

(b)

Fig. 13. (a) Perturbation velocity u at $y = 1.05$ for Case 6 (—) and Case 4 (- - -). (b) Wavenumber spectrum for u at $y = 1.05$ (Case 6).

limit of the computational domain did not extend to sufficiently low Reynolds number. Some fluctuations in the growth rates at the lower end of the *Re*-range indicate the influence of remnant CIFI near the leading edge of the panel. We have not been able to study the effects of boundary-layer growth on the CIFI modes because of the presence of significant TS wave components in all the cases that we have been able to examine to date.

5. Concluding remarks

The spatial-temporal evolution of small amplitude two-dimensional waves in Blasius boundary layer over finite-length viscoelastic compliant layer is numerically simulated in the present study. The numerical model employs a formulation in terms of streamfunction and vorticity, which ensures divergence-free solutions for the flow field.

On the whole, the computational results show that ribbon-generated TS waves grow more slowly over a finite viscoelastic compliant panel than similar waves of the same frequency over a rigid surface. The TS waves are generally modulated by CIFI or surface wave modes, which seem to gain greater prominence on a finite-length panel than on an infinite panel. On a finite-length panel, the leading and trailing edges of the compliant layer, as points of discontinuity in wall properties, appear to act as

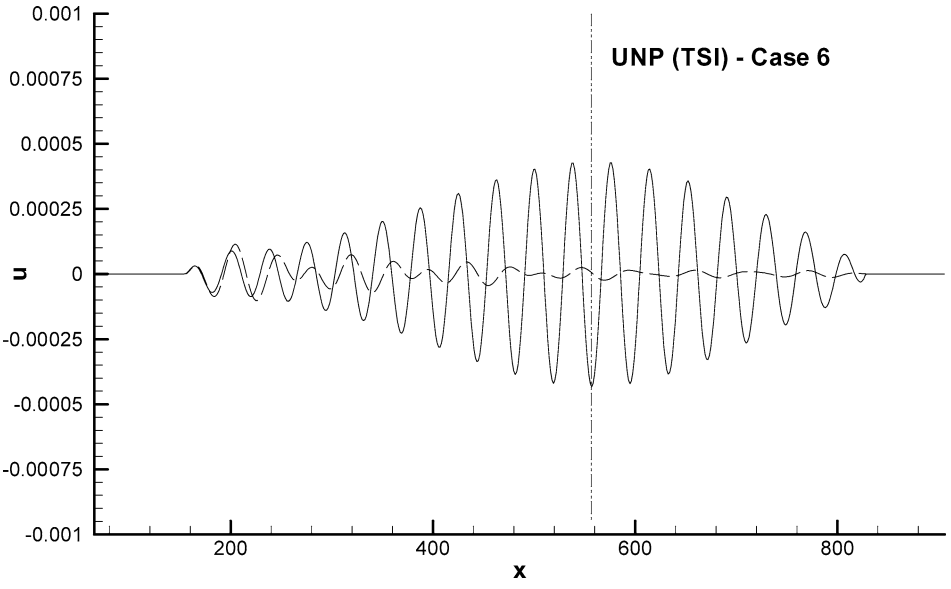

(c)

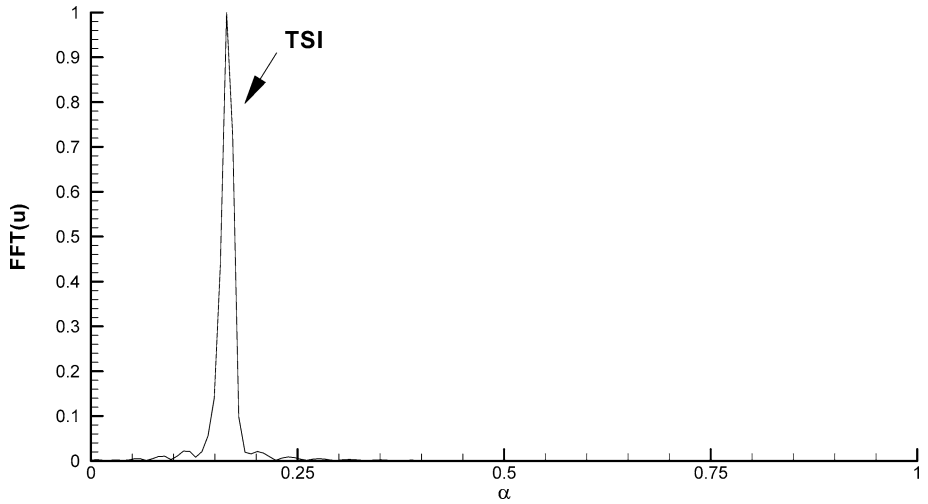

(d)

Fig. 13. (Continued). (c) Perturbation velocity u at $y = 0$ for Case 6 (—) and Case 4 (- - -). (d) Wavenumber spectrum for u at $y = 0$ (Case 6). Upper neutral point (UNP).

sources of surface waves when subjected to periodic wave perturbation by the flow. The results (Cases 1 and 2) show that CIFI modes that are damped or stable according to linear stability theory could be sustained in oscillation by leading edge excitation.

Increasing the thickness and/or reducing the shear modulus (stiffness) of the viscoelastic layer has the effect of causing the TS waves to grow more slowly or to decay more rapidly. The increase in compliance may, however, enhance existing CIFI modes and edge-related waves, or bring new ones into being. We found that CIFI modes and surface waves generated by the leading and trailing edges could be effectively and even completely suppressed by an increase in material damping (Case 6). The latter has an adverse effect on the TS waves. A judicious application of material damping is necessary in order to achieve suppression of CIFI and edge-related waves without unduly destabilizing the TS waves. The above behaviour of the TS and CIFI waves revealed through computational simulations is consistent with what is already known from linear stability analyses. Most of the observed waves and wave modes identified through spectral analyses of simulation results could be directly associated with eigenmodes of the linear stability theory. These results underline the continuing importance and relevance of linear stability theory as an analysis tool for compliant layer study, although, as the theory stands, it is unable to account for effects arising

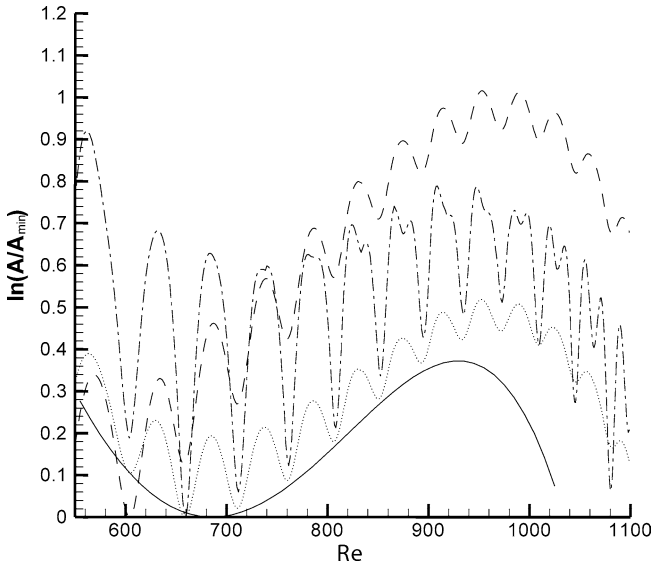

Fig. 14. Amplitudes of perturbation velocity u at different heights y (Case 2): — locally-parallel linear stability theory; $-\cdot-$ at $y=0$; $\cdots\cdots$ at $y=1$; - - - at $y=2$.

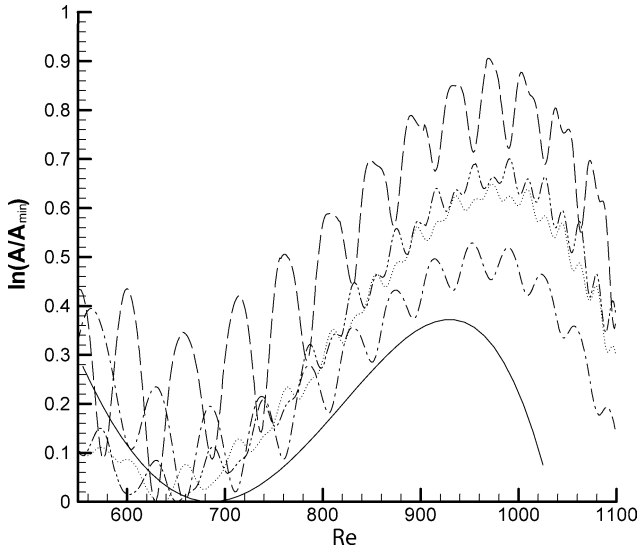

Fig. 15. Amplitudes of various maximum values (Case 2): — locally-parallel linear stability theory; $-\cdot-$ maximum u; $\cdots\cdots$ maximum v; - - - maximum ψ; $-\cdot\cdot-$ maximum ζ.

from property discontinuities at the panel edges. This explains the need for the application of direct numerical simulation in some situations at least.

Owing to spatial inhomogeneities introduced by panel edges and boundary-layer growth, it is not possible to decompose the wave response of the flow and surface into its constituent Fourier components in a precise manner. Furthermore, interference between waves gives rise to oscillations in the amplitude growth curves. These make it difficult for the neutral stability points of component modes to be located with any precision. However, the numerical evidence indicates that the lower and upper neutral branches of the TSI regime are shifted to lower and higher Reynolds numbers respectively compared to predictions of locally-parallel normal-mode analysis; or in other words, boundary layer growth over viscoelastic layers is destabilizing for the TSI.

The study also reveals two fairly distinct wave structures within the viscoelastic layers, which correspond to the propagation of the TSI and CIFI waves. These structures occur in pairs with opposite sense of rotation. The material displacement associated

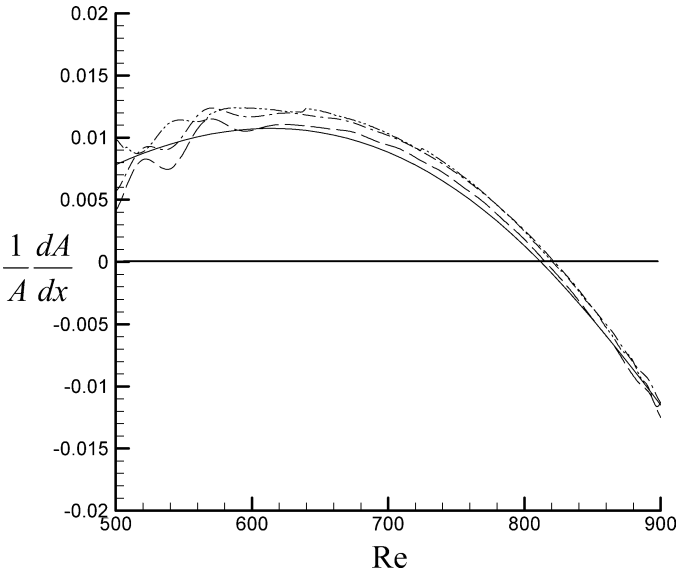

Fig. 16. Growth rates $A^{-1}\,\mathrm{d}A/\mathrm{d}x$ of different perturbation quantities (Case 6): — locally-parallel linear stability theory; - - - inner maximum u; $-\cdot-$ kinetic energy E; $-\cdot\cdot-$ maximum v.

with the longer wave, a the CIFI mode in all the cases considered here, extends through the full depth of the layer, whereas displacement structures related to the shorter wavelength (TSI) mode lingers near the surface.

Only the simplest, single-layer viscoelastic, finite-length compliant panels have been investigated in the present study. Viscoelastic materials tend to vary quite widely with regards to their damping response to periodic perturbations. We have adopted the simple Kelvin–Voigt damping model here, which may not be the appropriate model for many viscoelastic materials. Furthermore, the frequency and wavenumber response of a compliant surface may also be tailored or modified to a significant extent by explicit design, as Yeo [7] had shown for the case of viscoelastic multi-layer walls. The latter promises potential gains for flow stability and transition control, which need to be further explored by direct numerical simulation.

References

[1] T. Nonweiler, Qualitative solutions of the stability equation for a boundary layer in contact with various forms of flexible surface, Aeronaut. Res. Council Rep., CP622, 1963.
[2] R.E. Kaplan, The stability of laminar boundary layer in the presence of compliant boundaries, M.I.T., Sc.D. Thesis, 1964.
[3] M.T. Landahl, R.E. Kaplan, Effect of compliant walls on boundary layer stability and transition, AGARDograh 97 (1965) 363.
[4] L.A. Fraser, P.W. Carpenter, A numerical investigation of hydroelastic and hydrodynamic instabilities in laminar flows over compliant surfaces comprising of one or two layers of viscoelastic materials, in: Numerical Methods in Laminar and Turbulent Flows, Pineridge, 1985, p. 1171.
[5] K.S. Yeo, The stability of flow over flexible surfaces, Ph.D. Thesis, University of Cambridge, 1986.
[6] K.S. Yeo, A.P. Dowling, The stability of inviscid flow over passive compliant walls, J. Fluid Mech. 183 (1987) 265.
[7] K.S. Yeo, The stability of boundary-layer flow over single- and multi-layer viscoelastic walls, J. Fluid Mech. 196 (1988) 359.
[8] K.S. Yeo, The hydrodynamic stability of boundary-layer flow over a class of anisotropic compliant walls, J. Fluid Mech. 220 (1990) 125.
[9] K.S. Yeo, The three-dimensional stability of boundary-layer flow over compliant walls, J. Fluid Mech. 238 (1992) 537.
[10] K.S. Yeo, B.C. Khoo, W.K. Chong, The linear stability of boundary layer flow over compliant walls: effects of boundary layer growth, J. Fluid Mech. 280 (1994) 199.
[11] K.S. Yeo, B.C. Khoo, W.K. Chong, The linear stability of boundary layer flow over compliant walls – the effects of the wall mean state, induced by flow loading, J. Fluid Struct. 8 (1994) 529.
[12] K.S. Yeo, B.C. Khoo, H.Z. Zhao, The absolute instability of boundary-layer flow over viscoelastic walls, Theor. Comput. Fluid Dyn. 8 (1996) 237.
[13] K.S. Yeo, B.C. Khoo, H.Z. Zhao, The convective and absolute instability of fluid flow over viscoelastic compliant layers, J. Sound Vib. 223 (3) (1999) 379.
[14] K.S. Yeo, H.Z. Zhao, B.C. Khoo, Turbulent boundary layer over a compliant surface: absolute and convective instabilities, J. Fluid Mech. 449 (2001) 141.
[15] A.E. Dixon, A.D. Lucey, P.W. Carpenter, Optimization of viscoelastic compliant walls for transition delay, AIAA J. 32 (2) (1994) 256.

[16] K.S. Yeo, Optimization of viscoelastic compliant walls for transition delay, AIAA J. 36 (4) (1998) 656.
[17] J.A. Domaradzki, R.W. Metcalfe, Stabilization of laminar boundary layers by compliant membranes, Phys. Fluids 30 (3) (1987) 695.
[18] R.W. Metcalfe, F. Battistoni, S. Orzo, J. Ekeroot, Evolution of boundary layer flow over a compliant wall during transition to turbulence, in: Proceedings of Royal Aeronautical Society, 1991, 36.1.
[19] M.S. Hall, The interaction between a compliant material and an unstable boundary layer flow, J. Comput. Phys. 76 (1988) 33.
[20] C. Davies, P.W. Carpenter, Numerical simulation of the evolution of Tollmien–Schlichting waves over finite compliant panels, J. Fluid Mech. 335 (1997) 361.
[21] O. Wiplier, U. Ehrenstein, Numerical simulation of linear and non-linear Disturbance evolution in a boundary layer with complaint walls, J. Fluid Struct. 14 (2000) 157.
[22] O. Wiplier, U. Ehrenstein, On the absolute instability in a boundary-layer flow with compliant coatings, Eur. J. Mech. B Fluids 20 (2001) 127.
[23] C. Davies, P.W. Carpenter, A Novel velocity–vorticity formulation of the Navier–Stokes equations with applications to boundary layer disturbance evolution, J. Comput. Phys. 172 (2001) 119.
[24] Z. Wang, Computational simulation of unsteady boundary layer over compliant surfaces, Ph.D. Thesis, National University of Singapore, 2004.
[25] H.F. Fasel, Investigation of the stability of boundary layers by a finite-difference model of the Navier–Stokes equations, J. Fluid Mech. 78 (1976) 355.
[26] P. Giannattasio, M. Napolitano, Optimal vorticity conditions for node-centred finite-difference discretization of second-order vorticity–velocity equations, J. Comput. Phys. 127 (1996) 208.
[27] G. Guj, T. Stella, Numerical-solutions of high-Re recirculating-flow in vorticity velocity form, Int. J. Numer. Methods Fluids 8 (1998) 405.
[28] M. Napolitano, G. Pascazio, A numerical-method for the vorticity velocity Navier–Stokes equations in 2-dimensions and 3-dimensions, Comput. Fluids 19 (1991) 489.
[29] H. Fasel, U. Konzelmann, Nonparallel stability of a flat-plate boundary layer using the complete Navier–Stokes equations, J. Fluid Mech. 221 (1990) 311.
[30] C. Liu, Z. Liu, Multigrid mapping box relaxation for simulation of the whole process of flow transition in 3D boundary layer, J. Comput. Phys. 119 (2) (1995) 325.